PCCP
Physical Chemistry Chemical Physics

Accepted Manuscript

This article can be cited before page numbers have been issued, to do this please use: M. Kashif, S. I. A. Shah, S. Ahmad, S. U. Rahman, S. Azizi, S. Khan, M. Anwar and M. Malik, *Phys. Chem. Chem. Phys.*, 2025, DOI: 10.1039/D5CP02795K.

View Article Online
DOI: 10.1039/D5CP02795K

Bridging MOF and MXene: From Synthesis to Environmental and Energy Technologies

Muhammad Kashif[1], Syed Izaz Ali Shah[1], Salman Khan[1], Sheraz Ahmad[1], Muhammad Anwar[1], Sami Ur Rahman[1], Shohreh Azizi [2 *], Malik Maaza [2]

[1]*Department of Chemistry, Abdul Wali Khan University Mardan, Mardan 23200, Pakistan*

[2] *UNESCO-UNISA Africa Chair in Nanoscience and Nanotechnology College of Graduates Studies, University of South Africa, Muckleneuk Ridge, Pretoria, 392, South Africa*

[*]Corresponding author: Shohreh Azizi, Email: azizis@unisa.ac.za.

Abstract

Metal-organic frameworks (MOFs) and MXenes have emerged as complementary materials with distinct properties; MOFs offer tunable porosity and functional diversity, while MXenes provide strong electrical conductivity and surface reactivity. Their incorporation into MOF/MXene composites has performance across various environmental and energy applications. This study focuses on recent breakthroughs in the synthesis of MOF/MXene composites, including hydrothermal, green, self-assembly, and in-situ approaches. Furthermore, the applications of MXene/MOFs in dye and pharmaceutical degradation are thoroughly discussed. Moreover, the present work also elucidates the application in hydrogen production and supercapacitor development. The structure-function linkages and material design strategies are examined, giving insight into how the hybrids transcend their specific limits. Finally, key challenges and opportunities are identified to guide future research into scalable and efficient MOF/MXene-based technologies for sustainable environmental and energy systems. This work will contribute predominantly to the ongoing advancement in the MXene/MOFs hybrid design with applications in various technology sectors, including wastewater treatment, hydrogen production and supercapacitors.

Keywords: MOF/MXene composites; Photocatalysis; Environmental remediation's; Hydrogen production; Supercapacitors

View Article Online
DOI: 10.1039/D5CP02795K

1. Introduction

Environmental pollution has emerged as a significant global concern in recent years.[1] This growing issue encompasses the contamination of soil, water, and air.[2] Rapid industrialization has significantly increased the production of hazardous organic contaminants, thereby exacerbating pollution in the soil, water and air. Among the primary contributors to environmental pollution, particularly water contamination, are industrial effluents, which include inorganic metal ions, synthetic dyes, aromatic and aliphatic compounds, agricultural residues such as fertilizers and pesticides, pathogenic microbes, and pharmaceutical byproducts.[3, 4] Such pollutants pose a significant threat to the global ecosystem, with persistent organic pollutants being particularly concerning due to their longevity and bioaccumulation potential.[5] Historically, dyes were derived from natural sources, such as vegetables, flowers, wood, roots, and insects, until the introduction of synthetic alternatives in 1856.[6] Natural dyes are considered environmentally benign because they degrade easily under sunlight, leaving a minimal ecological footprint. However, the rapid growth of industries such as food processing, plastics, textiles, and cosmetics has escalated the demand for dyes, prompting the widespread adoption of synthetic alternatives to meet this need. Synthetic dyes are crucial to these industries as they offer advantages such as high availability, cost-efficiency, colorfastness, and resistance to light, pH fluctuations, and oxidation. Globally, around 80,000 tons of synthetic dyes are produced each year, yet only about 80% are utilized in the dying process; the remaining 10-15% enter wastewater systems as residual pollutants.[7]

In addition to synthetic dyes, pharmaceutical compounds also contribute significantly to water pollution, posing a serious environmental concern. These pharmaceutical contaminants originate from various sources, including prescription drugs, over-the-counter medications, and veterinary medications. While substances play a crucial role in treating numerous health conditions, their

View Article Online
DOI: 10.1039/D5CP02795K

unintended release into the environment poses long-term risks. Pharmaceutical substances fall into several categories, including antiviral (Tamiflu), antidepressant (alprazolam), antiepileptic (carbamazepine), analgesics like naproxen and ibuprofen, antibiotics such as nitrofurantoin, levofloxacin, chloramphenicol (CAP), and hormonal agents estriol and 17-β estradiol.[8] These chemicals are released into the environment through multiple pathways, including human excretion, livestock waste, hospital effluents, municipal wastewater, improper disposal practices, and industrial discharge from pharmaceutical manufacturing.[9] As a result, untreated human waste containing pharmaceutical residues often leaches into nearby freshwater bodies.[10] One prominent example is the transformation of male fish into female ones due to the development of feminine qualities. Estrogens in the water can also reduce male fertility and may increase the risk of testicular and breast cancer.[11-13] Additionally, anti-cancer drugs found in drinking water are capable of crossing the placental barrier, causing teratogenic and embryotoxic effects. These cytotoxic pharmaceuticals are hazardous for pregnant women due to their potential to disrupt embryonic development.[14-16] Effective removal of organic pollutants from contaminated water is essential for ensuring safety. Water purification involves eliminating contaminants from wastewater to make it suitable for reuse. Traditional treatment methods, such as solvent extraction, ion exchange, chemical precipitation, adsorption, distillation, membrane filtration, and sedimentation, primarily transfer pollutants between phases rather than degrade them, often generating concentrated sludge and incurring high operational costs. In contrast, advanced oxidation processes (AOPs) have emerged as highly effective method for removal of organic contaminants. Key AOPs include UV/H_2O_2, UV/S_2O_8, UV/O_3, UV/TiO_2, O_3/H_2O_2, Fe_3O_4/H_2O_2, gamma irradiation, electron beam treatment, and various photocatalytic and electrochemical approaches.

View Article Online
DOI: 10.1039/D5CP02795K

Currently, fossil fuels account for approximately 80% of global energy consumption, although their dominance is gradually declining.[17] However, energy production from fossil fuels contributes substantially to greenhouse gas emissions, particularly CO_2, which accelerates climate change.[18, 19] As CO_2 and other greenhouse gas emissions continue to rise, the risks associated with global warming and climate instability are escalating. To mitigate these impacts, a transition toward renewable energy sources and stronger climate policies is essential.[20] For example, in Hong Kong, direct fossil fuel use in electricity generation and transportation accounts for 48% and 36% respectively, of the estimated 290,000 TJ annual energy consumption.[21] Furthermore, fossil fuel-based energy systems emit a wide range of harmful pollutants, including heavy metals, ashes, radioactivity, SOx, NOx, CO_2, etc., at levels far greater than those produced by hydrogen energy systems based on renewable sources.[22] The International Energy Agency (IEA) forecast that CO_2 emissions from the energy sector will rise from 50% in 2030 to 80% in 2050.[23] This pursuit of alternative energy sources has accelerated notably since the 1973 oil crisis, which highlighted the vulnerabilities of fossil fuel dependence.[24] The rapid advancement of the electronics industry and the increasing integration of electronic devices into daily life have spurred the development of clean and renewable energy storage and conversion technologies.[25] As a response to global energy challenges, these efficient storage and conversion of energy have become a defining aspect of technological evolution in the modern world. Among these, supercapacitors are gaining increasing recognition due to their high-power density, long life cycle, and rapid charge discharge capabilities. Supercapacitors are generally classified into electrical double-layer capacitors (EDLCs) and pseudo-capacitors, based on their charge storage mechanisms.[26] EDLCs typically utilize carbon-based electrode materials to form an electrostatic double layer at the electrode-electrolyte interface, enabling energy storage through physical ion adsorption. In contrast, pseudo-

View Article Online
DOI: 10.1039/D5CP02795K

capacitors rely on fast and reversible faradaic redox reactions using conducting polymers and metal oxide derivatives to generate electrochemical energy in the presence of applied potential.[27] Therefore, selecting appropriate electrode materials is critical for optimizing supercapacitor performance.

In earlier studies, a wide variety of materials were employed as supercapacitor electrodes, including conducting polymers, metal hydroxides, metal chalcogenides, MXenes, graphene, and various metal oxides. The development of cost-effective materials based on non-precious metals with high product selectivity and catalytic activity is essential for advancing photocatalysis.[28, 29] Metal-organic frameworks (MOFs), which are crystalline porous materials are synthesized by coordinating metal ions or clusters with organic ligands.[30, 31] The growing interest is attributed mainly to their remarkable features, such as high surface area, variable crystalline structures, flexible chemistry, changeable bandgap.[32, 33] Recent studies have demonstrated that the unique layered structure of two-dimensional MXenes enhances photocatalytic hydrogen production and facilitates their integration with other semiconductors as co-catalysts. These materials have been proposed as an effective alternative to noble-metal catalysts, owing to their comparable catalytic properties.[34, 35] Among them, titanium carbide (Ti_3C_2) stands out due to its excellent stability, ease of fabrication, enhanced catalytic activity, and the presence of surface functional groups. MXenes possess high electrical conductivity, their standalone photocatalytic efficiency remains limited. Therefore, they are often employed as a co-catalyst when combined with semiconductors to improve overall system performance. One such example is the incorporation of Ti_3C_2 MXenes with metal organic frameworks (MOFs), forming synergistic composite systems. However, the intrinsic susceptibility of MXene, particularly $Ti_3C_2T_{x,}$ to surface oxidation under ambient conditions remains a major barrier to their practical deployment. Recent advances, have

View Article Online
DOI: 10.1039/D5CP02795K

demonstrated promising stabilization strategies through both chemical modification and protective coatings. For instance, surface engineering with Al_2O_3 via atomic layer deposition has been shown to form conformal oxides shells that effectively inhibit oxidation without impairing electrical conductivity.[36] Similarly polymer encapsulation using conductive polymers such as polyaniline and PEDOT has improved both environmental durability and electrochemical performance by passivating surface -OH and -F groups, thereby reducing reactive sites for oxidative attack.[37] Beyond polymer coatings, heterostructure construction has emerged as another visible route: embedding MXene within MOF or carbonaceous frameworks provides physical shielding and additional interfacial stabilization, significantly prolonging structural integrity under humid and oxygen-rich environments.[38] Aqueous processing modifications have also been reported, where optimized pH and antioxidant additives (e.g., ascorbic acid) suppress oxidative degradation during storage and handling.[39] More recently, hybrid coatings combining inorganic oxides with carbon layers have delivered synergistic protection, balancing diffusion barrier properties with enhanced electron transport.[40] Therefore, materials with high electrical conductivity and strong ability to capture and transport photo-induced charge carriers are critical for addressing the inherently low conductivity of MOFs. Ti_3C_2 MXenes fulfil this role effectively due to their outstanding conductivity and structural stability.[41] Furthermore, the interfacial interactions between MOFs and MXenes are key to their composite performance, involving hydrogen bonding, electrostatic forces, and van der Waals interactions between MOF functional groups and MXene surface terminations. Strong interfaces enhance charge transfer, stability, and catalytic activity. Advanced techniques like HRTEM, XPS, and AFM help probe these interactions at the nanoscale, guiding the design of high-performance composites. Despite their promise, MXene-based MOF composites tailored for

View Article Online
DOI: 10.1039/D5CP02795K

photocatalytic water splitting remain relatively underexplored. Figure (1) illustrates different timelines of MXene and MOFs composites along with their related publications.

View Article Online
DOI: 10.1039/D5CP02795K

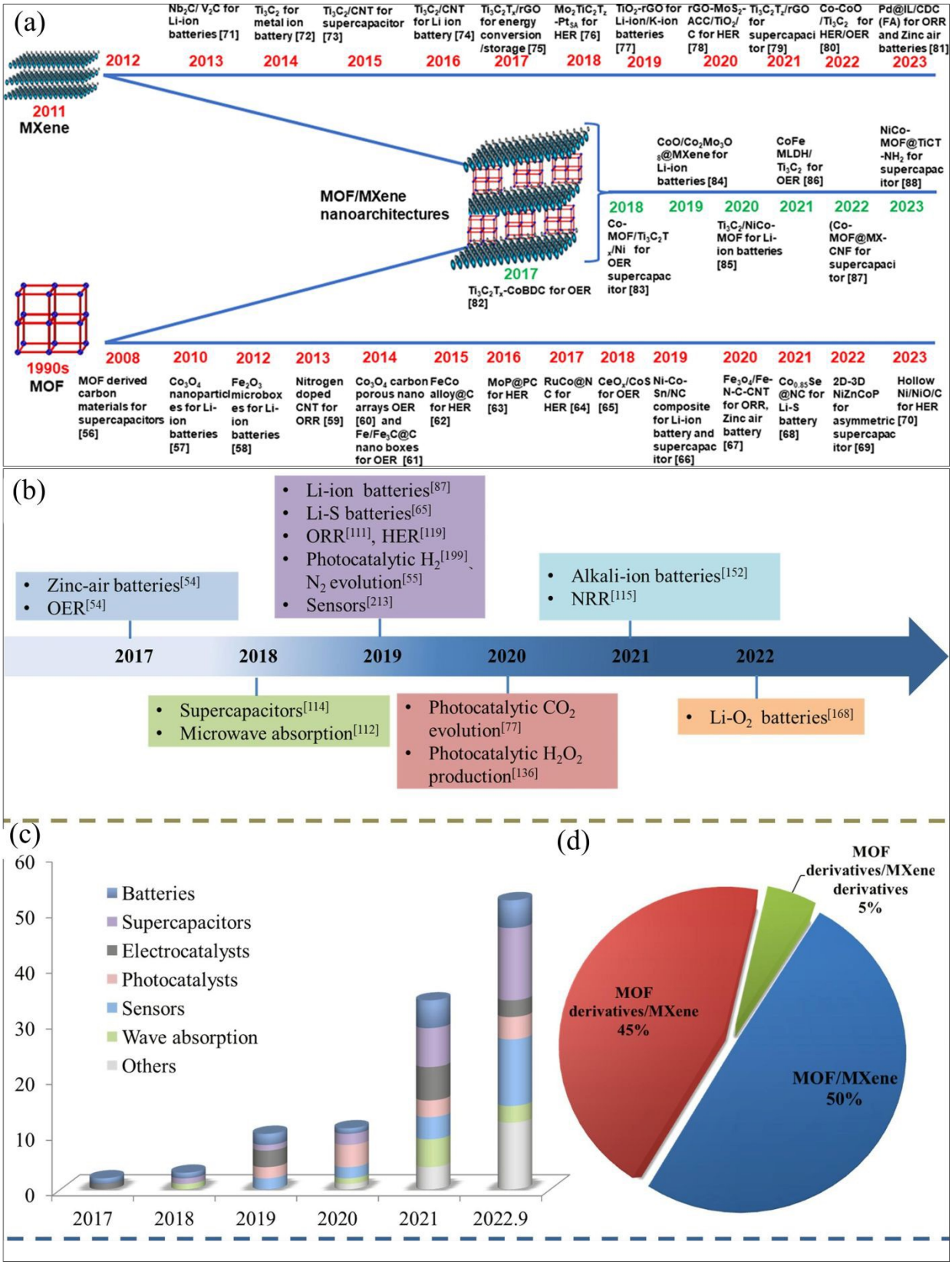

View Article Online
DOI: 10.1039/D5CP02795K

Figure 1. (a) Chronology of significant advancements in MOF, MXene, and MOF/MXene nanocomposites for electrochemical energy conversion and storage. Reproduced with permission from.[42] Copyright 2023, Elsevier, (b) Timeline of the initial reports of different MOF/MXene-based composite uses (c) publications on different uses of MOF/MXene throughout the years (d) Pie chart showing the classification of MOF/MXene-based composites with time. Reproduced with permission from.[43] Copyright 2023, Elsevier.

This review presents recent advancements in MOF/MXene composite, emphasizing their synthesis methods, structural features, and multifunctional applications. Particular focus is given to their roles in environmental remediation, sustainable hydrogen production through water splitting and high-performance supercapacitors. The integration of MOFs high porosity and tunable chemistry with MXenes excellent conductivity and mechanical strength imparts superior physiochemical characteristics to the composites. By addressing current challenges and future directions, this review offers valuable insights for the rational design MOF/MXene composites in energy and environmental fields.

2. Synthesis method

The synthesis of MOF/MXene composites plays a pivotal role in determining their structural integrity, surface functionality, and overall performance in various applications. Several synthesis strategies have been developed to combine the unique properties of MOFs and MXenes effectively. These methods are designed to ensure strong interfacial interactions, uniform dispersion, and optimized composite architectures. Commonly employed techniques include hydrothermal and solvothermal synthesis, which facilitate the growth of MOFs on the MXene surface under controlled temperatures and pressure conditions. In –situ synthesis enables the direct formation of MOF structures in the presence of MXene, promoting intimate contact at the molecular level. Furthermore, green synthesis methods have gained attention for their environmentally friendly approach, utilizing non-toxic solvents and mild conditions. Additionally, electrostatic attraction methods leverage surface charge interactions to assemble MOF and MXene

View Article Online
DOI: 10.1039/D5CP02795K

components effectively. Each of these synthesis approaches offers distinct advantages and challenges (Table 1), which are discussed in detail in the following sections.

Table 1. Summary of different synthesis methods of MXene/MOFs composites.

Synthesis Method	**Key Features**	**Advantages**	**Limitations**	**Typical Applications**
Hydrothermal	High temperature/pressure, aqueous-based	Simple, high crystallinity, good morphology control	Long reaction time, energy-intensive	Photocatalysis, adsorption
Solvothermal	Organic solvent-based, high temp/pressure	Wide range of morphologies, high product yield	Solvent toxicity, costly solvents	Catalysis, sensors
In-situ	MOF grows in presence of MXene	Strong interface bonding, simple procedure	Requires careful control of conditions	Hybrid materials, energy storage
Green synthesis	Eco-friendly solvents, mild conditions	Environmentally benign, cost-effective	Limited to certain MOFs, lower crystallinity	Catalysis, biomedical
Electrostatic self-assembly	Surface charge-driven assembly	Mild conditions, good dispersion	Less stable under harsh conditions	Photocatalysis, electronics

2.1 Hydrothermal/solvothermal method;

Hydrothermal/solvothermal synthesis methods offer a straightforward approach for fabricating a nanocomposite with controlled morphologies.[44, 45] Typically, hydrothermal synthesis promotes the formation of dynamic frameworks, characterized by permanent metal-ligand linkage across the structure.[46, 47] Under these conditions, single crystal forms within reactors, guided by the materials decomposition rate in hot water under high vapor pressure at elevated temperatures. In contrast, the solvothermal technique uses a solvent other than water to enable materials synthesis. While both methods aim to produce high-quality crystalline products, they typically

View Article Online
DOI: 10.1039/D5CP02795K

operate under moderately elevated temperature conditions.[48] These methods typically involve the reaction of metal salts or metal complexes in water or solvents, heated under high pressure and temperatures within an autoclave. Under standard conditions, these reactions proceed over 6 to 48 h, during which disintegration, granulation and crystallization of poorly soluble compounds occur.[49] Among these methods, the solvothermal approach is particularly favored for synthesizing MOFs due to its ability to yield a wide range of morphologies. This method involves reacting an organic ligand with a metal salt in either a solvent mixture or pure organic solvents. Commonly used solvents include acetone, diethyl formamide, methanol, and acetonitrile.[50] When MOF and MXene precursors react under high-temperature solvothermal conditions and self-generated pressure, the process achieves high product yield and remains operationally simple. This technology is especially valuable for controlling the morphology of hybrid materials and fabricating hierarchical architectures.[51] For example, Tian et al.[52] fabricated Ti_3C_2/TiO_2/UiO-66-NH_2 nanocomposite through the solvothermal method **(Figure 2a).** The process began with stirring the solution for 1 h, after which 2 weight percent of TCA was added to the $ZrCl_4$ solution. Subsequently, BDC-NH_2 was added to the suspension, followed by an additional 30 min of stirring. The resulting mixture was transferred into an autoclave and heated at 120 °C for 24 h. After natural cooling, the precipitates were washed with (DMF) to remove unreacted organic ligands, followed by solvent exchange with anhydrous methanol. Finally, the yellow Ti_3C_2/TiO_2/UiO-66-NH_2 product was isolated by centrifugation and dried under vacuum at 80 ℃ for 12 h. Similarly, Yu et al.[53] manufactured the photocatalyst, designated MPA-m/U66N-M via a hydrothermal method **(Figure 2b).** Initially, zirconium tetrachloride ($ZrCl_4$) was completely dissolved in DMF, forming what was referred to as solution A. Once dissolution was complete, the organic molecule MPA-m was added to solution (A), and the mixture was stirred continuously

View Article Online
DOI: 10.1039/D5CP02795K

for one hour to ensure proper interaction. In parallel, H_2ATA was dissolved in a separate portion of DMF to form solution (B). Following 30 minutes of stirring, acetic acid was added to the mixture to facilitate the coordination reaction. The combined solution was subsequently transferred into a reactor and subjected to micro-assisted hydrothermal treatment at 120 °C for 40 min under 300 W of microwave radiation. After the reaction, the synthesized product was isolated by centrifugation, followed by repeated washing with methanol and DMF to remove unreacted species. Finally, the purified product was dried under vacuum overnight at 80 °C. In another study, Tian et al.[54] synthesized Ti_3C_2@UiO-66-NH_2 nanocomposite using a hydrothermal technique, as illustrated in (**Figure 2c).** Initially, a mixed solution of $ZrCl_4$ in DMF and HCl was prepared, referred to as solution (A). Ti_3C_2 nanosheets were then added to the solution (A), followed by stirring for 1 h to ensure uniform dispersion. In a separate step, BDC was dissolved in DMF to form solution (B), which was then gradually added to solution (A). The combined solution was transferred to an autoclave and subjected to hydrothermal treatment at 120 ℃ for 24 h. After cooling, the resulting products were collected by centrifugation, thoroughly washed with ethanol and DMF, and then dried at 60℃ for 12 h. Additionally, Yang et al.[55] employed a hydrothermal method to synthesize the MX@MIL-125(Ti) nanocomposite. In this synthesis, BDC acted as the organic linker, while the previously prepared Ti_3C_2 MXene served as the titanium source. To begin, BDC was dissolved in a solvent mixture of DMF and methanol, and the mixture was stirred continuously before the addition of Ti_3C_2 MXene. Following this, the resulting solution was transferred into an autoclave and heated to 150 °C to initiate the hydrothermal reaction. After 24 h, the suspension was collected, allowed to cool to room temperature, and centrifuged at high speed to separate the solid product by removing the supernatant. To obtain the final MX@MIL-125(Ti) nanocomposite, the precipitate was repeatedly cleaned with fresh methanol and dried.

View Article Online
DOI: 10.1039/D5CP02795K

Furthermore, Shalini et al.[56] prepared the MN-MX nanocomposite using a hydrothermal approach, as depicted in **Figure 2d.** Initially, the pre-synthesized MX was dispersed in DMF and sonicated for 30 min to ensure proper exfoliation and dispersion. Simultaneously, BDC and ethanol were added to a separate mixture and stirred for 15 minutes until fully dissolved. Subsequently, [Ni (CH_3COO) and [Mn (CH_3COO) $2.4H_2$ $2.4H_2O$] O] were added into the BDC solution, stirred for 30 minutes after complete dissolution. The resulting metal-ligand solution was then poured into the previously sonicated MX solution. To achieve uniform distribution, the combined solution was stirred again for 30 minutes. The homogeneous solution was then transferred into an autoclave lined with Teflon and heated at 180 °C for 24 h under static conditions. After cooling to room temperature, the resulting light green precipitate was collected and washed with DI water and ethanol. The purified product was then ground using an agate mortar, designated as 25 MX-MN and dried at 60 °C for 12 h.

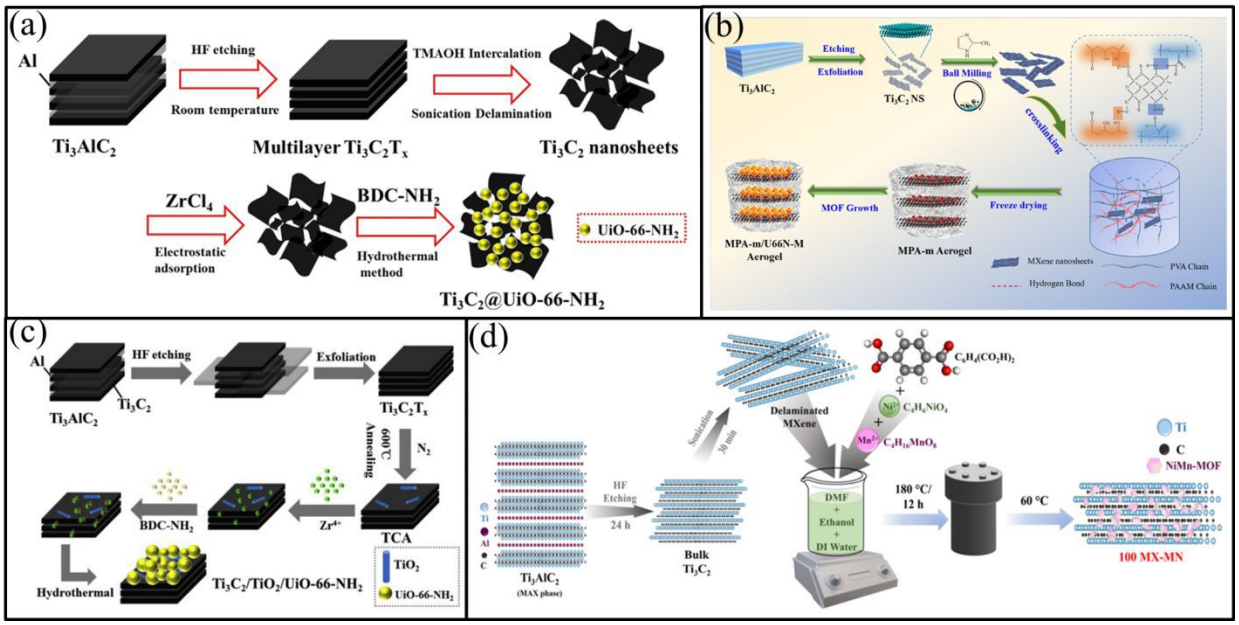

View Article Online
DOI: 10.1039/D5CP02795K

Figure 2. (a) Schematic depiction of a proposed chemical route for synthesis of Ti_3C_2/TiO_2/UiO-66-NH_2. Reproduced with permission from.[52] Copyright 2019, Elsevier, (b) a demonstration of MPA-m/U66N-M synthesis method. Reproduced with permission from.[53] Copyright 2023, Elsevier, (c) scheme illustration for preparing Ti_3C_2 nanosheets and TU series. Reproduced with permission from.[54] Copyright 2019, Elsevier, **(d)** Schematic representation of etching of aluminum from the MAX phase and production of composites. Reproduced with permission from.[56] Copyright 2024, Elsevier.

Liu et al.[57] synthesized Ti_3C_2Tx vs MIL-53(Fe) hybrid materials by adjusting the mass ratio of Ti_3C_2Tx to MIL-53(Fe) through a practical solvothermal approach. Initially, a predetermined amount of Ti_3C_2Tx powder was dispersed in DMF using ultrasonic treatment for 2 h to ensure uniform dispersion. Subsequently $FeCl_3 \cdot 6H_2O$, and H_2BDC, were added to the Ti_3C_2Tx suspension, and the mixture was stirred until a homogenous solution was obtained. The resulting solution was then transferred into an autoclave and subjected to solvothermal treatment at 150 °C for 24 h. Post-synthesis treatment steps were conducted following the same procedure as used for MIL 53(Fe) synthesis. Similarly, Lin et al.[58] synthesized MIL-101(Fe)/g-C_3N_4 nanocomposites (MCN) via a hydrothermal method. Initially, the g-C_3N_4 nanosheets were uniformly dispersed in a MIL-101(Fe) precursor solution. The resulting mixture was stirred for 3 h, followed by hydrothermal treatment at 120 °C for 20 h. The obtained brown powder was washed with methanol and vacuum-dried for 12 h at 60 °C. To synthesize MXene@MIL-101 (Fe)/g-C_3N_4 nanocomposite (MX@MCN), **(Figure 3a)** the MCN powder was mixed with methanol for 10 min. Subsequently, MXene nanosheets were gradually added to the mixture and stirred for an additional hour. After methanol washing, the resulting solid was freeze-dried for 3 days to yield MX8%@MCN_3 powder.

2.2 Synthesis of MOF/MXene composite through a green approach

View Article Online
DOI: 10.1039/D5CP02795K

Eslaminejad et al.[59] synthesized a Pd/MXOF nanocomposite using an environmentally friendly green approach **(Figure 3b).** The preparation of MXene/MIL-101(Fe) (MXOF) involves several sequential steps. Initially, MXene powder was ultrasonically dispersed in DMF for 120 min, resulting in what was referred to as Mixture 1. Separately, mixture 2 was synthesized by dissolving $FeCl_3 \cdot 6H_2O$, and H_2BDC, in DMF. These two mixtures were then combined and stirred together for 20 min to initiate the coordination process. The resulting homogenous solution was transferred to an autoclave and heated at 110 °C for one day to facilitate crystallization. To fabricate the Pd/MXOF nanocomposite, the obtained MXOF was first dispersed in ethanol using a bath sonicator. Following this, $Pd(NO_3)_2 \cdot 2H_2O$ was added into the dispersion. Subsequently, an ethanolic solution of propolis was added dropwise into the suspension under a nitrogen atmosphere. The entire suspension was stirred at ambient temperature for 24 h to ensure uniform deposition and reaction. Finally, the resulting black precipitate was collected, washed with ethanol and water, and dried overnight at 60 ◦C.

2.3 MOF/MXene synthesis via an electrostatic self-assembly approach

Various non-covalent interactions, including electrostatic interaction, pi-pi stacking, and hydrogen bonding, can collectively drive self-assembly, leading to the spontaneous organization of components into an ordered structure.[60, 61] For example, Cheng et al.[62] employed an electrostatic self-assembly method to synthesize the UNiMOF/Ti_3C_2 nanocomposite **(Figure 3c).** In the first step, solution A was prepared by dissolving (BDC) in a solvent mixture containing ethanol, DMF, and DI water. Subsequently, $NiCl_2 \bullet 6H_2O$ was introduced into the solution under vigorous stirring for 30 minutes to promote precursor interaction. In parallel, suspension B was prepared by dispersing a specific amount of Ti_3C_2 nanosheets in DI water. Suspension B was then gradually added dropwise into solution A while maintaining continuous magnetic stirring. After 30 minutes

View Article Online
DOI: 10.1039/D5CP02795K

of stirring, (TEA) was rapidly added to the reaction mixture to facilitate nucleation and growth. The mixture was subjected to ultrasonic treatment at 40 Hz for 4 h. After the reaction, the solid product was collected via centrifugation to remove the solvent. The precipitate was washed three times with DMF, and ethanol, and dried overnight at 90 °C. Liu et al.[63] employed an electrostatic attraction approach to prepare Ti-MOF/QDs/ZIS nanocomposite **(Figure 3d).** Briefly, Ti-MOF/ZIS was ultrasonically dispersed in distilled water. Following this, the dispersion was purged with nitrogen gas for 60 minutes to remove dissolved oxygen. A specific amount of Ti dots (QDs) derived from MXene was then added to the oxygen-free dispersion. At pH 7, the MXene QDs are negatively charged, whereas the Ti-MOF/ZIS surface carries a positive charge thereby facilitating electrostatic assembly. The mixture was then stirred continuously at 35 °C for 12 h under a N_2 environment. Finally, the resulting Ti-MOF/QDs/ZIS composite was obtained by filtration, followed by washing the filtered material three times with DI water. The residual solvent was then removed via vacuum distillation to obtain the product.

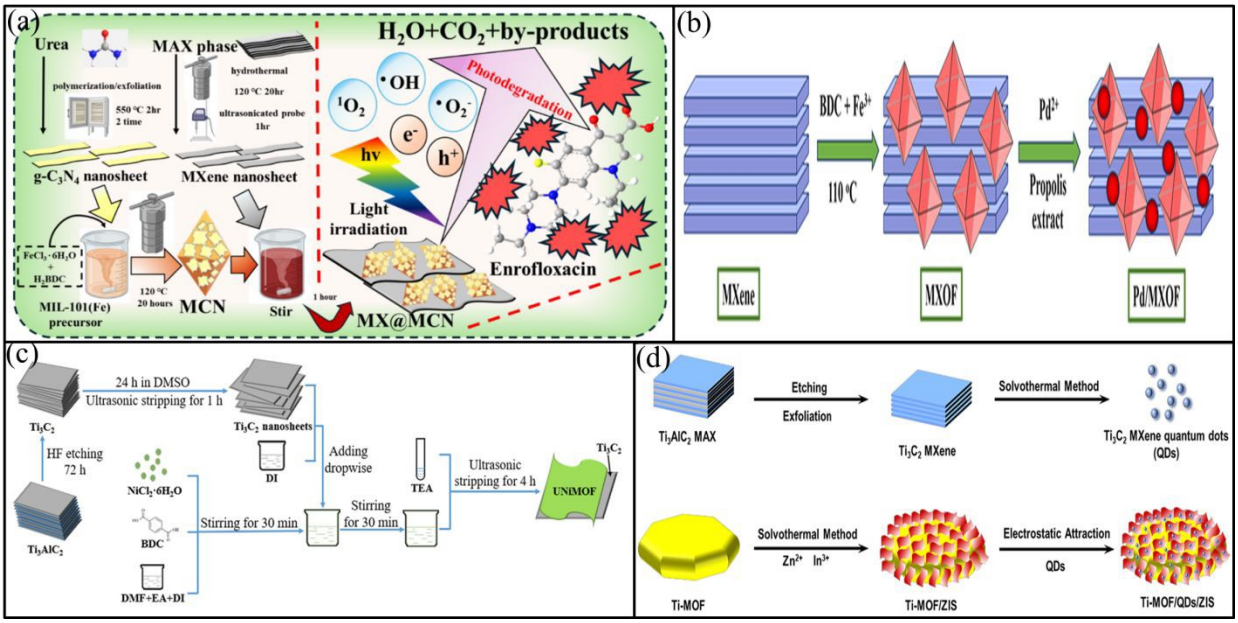

View Article Online
DOI: 10.1039/D5CP02795K

Figure 3. (a) Description of the production of MX@MCN and its photocatalytic activity to degrade enrofloxacin through light. Reproduced with permission from.[58] Copyright 2025, Elsevier, (b) schematic description for synthesis of Pd/MXOF photocatalyst. Reproduced with permission from.[59] Copyright 2025, Elsevier, (c) Fabrication procedure of the UNiMOF/Ti_3C_2 composites. Reproduced with permission from.[62] Copyright 2021, Elsevier, (d) Schematic representation synthesis of Z-Scheme NH_2-MIL-125 (Ti)/Ti_3C_2 MXene quantum dots $ZnIn_2S_4$ composites (Ti-MOF/QDs/ZIS). Reproduced with permission from.[63] Copyright 2022, Elsevier.

2.4 Synthesis of MOF/MXene through in situ method

Due to spontaneous formation, the bonding at the composite interface tends to be relatively strong. Moreover, this strategy simplifies the synthesis process by eliminating the need for complex, multi-step procedures.[64] Among the commonly employed fabrication methods, in-situ synthesis remains one of the most widely adopted techniques for composite formation.[65] In the case of MOF/MXene composites, this approach involves adding MXenes into a solution of organic ligands and well-dissolved metal ions. Importantly, this procedure follows the same synthetic route typically used for MOFs themselves. "The term same synthesis method" refers to a variety of techniques, including the hydrothermal method, ambient temperature diffusion-assisted interdiffusion reaction and others. Among these, the ambient temperature diffusion method is particularly notable for its simplicity and environmentally friendly conditions, making it both cost-effective and user-friendly.[66] For example, He et al.[67] employed an in-situ synthesis method to fabricate Ti_3C_2/UiO-66-NH_2 Composites **(Figure 4a).** The synthesis began by dissolving $ZrCl_4$ in a solvent of DMF and acetic acid, after which a measured quantity of Ti_3C_2 was added to the solution. After stirring the mixture for 1 h, pre-dissolved BDC-NH_2 in DMF was added, and the combined solution was stirred for an additional 30 minutes. The resulting mixture was then

View Article Online
DOI: 10.1039/D5CP02795K

transferred to an autoclave and heated at 120 °C for 24 h to promote crystallization. After cooling naturally to room temperature, the precipitate was washed with anhydrous methanol and DMF. The yellow precipitates were then vacuum-dried for an entire night at 80 °C and subsequently labeled according to their Ti_3C_2 contents 5 weight percent Ti_3C_2/UiO-66-NH_2, 10 weight percent Ti_3C_2/UiO-66-NH_2, 15 weight percent Ti_3C_2/UiO-66-NH_2, and 20 weight percent Ti_3C_2/UiO-66-NH_2, which are shorthand for 1-T/U, 2-T/U, 3-T/U, and 4-T/U, respectively. Far et al.[68] prepared MXene@UiO-66 nanocomposite through an in-situ method. In this process, UiO-66 crystals were uniformly assembled on the surface of MXene nanosheets **(Figure 4b).** To begin, $ZrCl_4$ and the TPA ligand were dissolved in DMF at room temperature in the presence of MXene powder, followed by sonication for 15 min. The resulting solution was then transferred into an autoclave and heated at 120℃ for a day. After cooling, the grey products were collected and washed three times with DI water. Finally, the MXene@UiO-66 was dried at 80°C for 6 h.

View Article Online
DOI: 10.1039/D5CP02795K

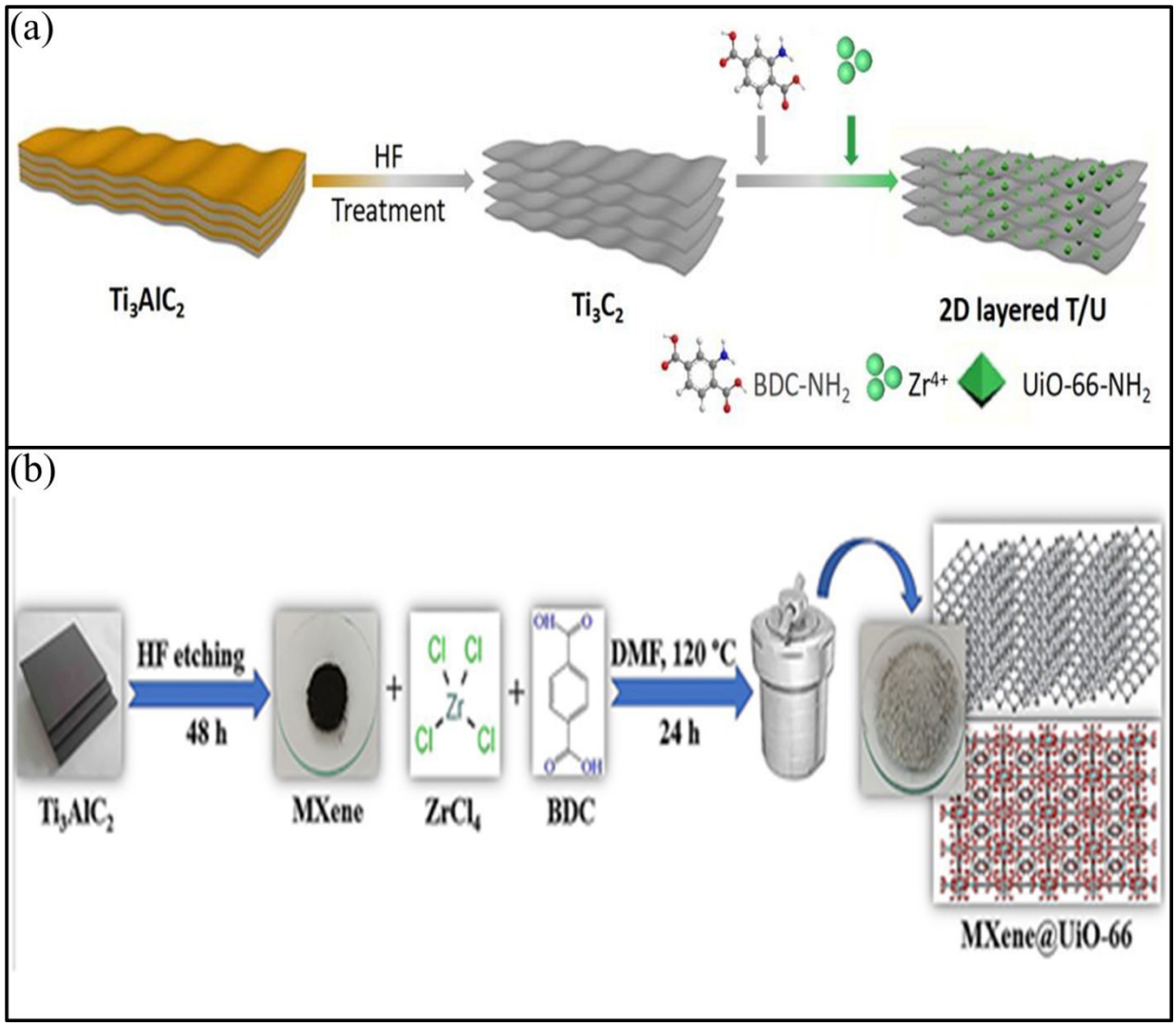

Figure 4. (a) Schematic diagram for Ti_3C_2 MXene and Ti_3C_2/UiO66NH_2 composites preparation. Figure reproduced from.[67] which is open access and permits unrestricted use of materials under the terms of the Creative Commons CC-BY, (b) schematic depiction of the method for synthesizing of MXene@UiO-66 nanocomposite. Reproduced with permission from.[68] Copyright 2024, Elsevier.

Far et al.[69] synthesized the MXOF composite through an in-situ method involving the formation of MOF in the presence of MXene. Initially, zinc nitrate and 2-MIM were separately dissolved in methanol in two separate containers. Subsequently, MXene powder was added to the 2-MIM

View Article Online
DOI: 10.1039/D5CP02795K

solution and sonicated for five minutes to disperse it. The zinc nitrate solution was then added dropwise to the MXene-containing 2-MIM solution under continuous stirring at 35 °C for three h. The resulting product was collected by centrifugation and washed three times with DI water. Finally, the grey powder was subsequently dried for six h at 80 °C.

2.4. From Lab to Industry: MOF Scale-Up Challenges

Scaling up the synthesis of MOF- based and hybrid materials from the laboratory demonstrations to industrial implementation remains a formidable challenge, requiring careful consideration of both economic and technical barriers. At the laboratory scale, solvothermal and hydrothermal methods dominate due to their ability to yield highly crystalline products with tunable structures. However, these techniques often rely on high temperatures, long reaction times, and toxic organic solvents, which significantly hinder large- scale deployment due to environmental, safety, and cost concerns.[70, 71] One major bottleneck is the transitions to green and scalable synthesis routes such as mechanochemical, electrochemical, and spray-drying strategies, which can minimize solvent usage and reduce energy demand. While mechanochemical synthesis has been demonstrated as a scalable and eco-friendly pathway, reproducibility and control over particle size distribution at industrial throughput remain unresolved.[72] Similarly, continuous flow and microreactor-assisted synthesis offer advantages in automation and uniformity but are yet to be optimized for producing large batches without compromising structural integrity.[73] Another challenge lies in the high cost of ligands and metal precursors, particularly for rate earth or noble metal-based framework. Although efforts have been made toward replacing expensive linkers with bio-derived or waste-sourced precursors, such approaches are still underexplored at scale [74]. In addition, maintaining crystallinity porosity and functionality when shifting from gram –scale to kilogram scale production is nontrivial. For instance defects inter particle aggregation and morphology

View Article Online
DOI: 10.1039/D5CP02795K

inconsistencies frequently appear in called up batches which directly affect electrochemical or catalytic performance.[75] The integration of conductive dopants or hybridization with carbonaceous nanomaterials introduce further complexity. While doping strategies enhance conductivity and electrochemical stability at small scale achieving homogenous distribution across kilogram-scale batches is difficult and often results in performance variations.[76] Moreover, the scalability of post-synthetic modifications such as doping, surface functionalization or hybrid composite fabrication remains uncertain due to multi-step processing and high solvent consumption.[77] From an industrial perspective, energy and environmental footprints are also critical. Large scale solvothermal synthesis not only demands substantial thermal energy but also generates significant volumes of solvent waste, which raises issues regarding sustainability and compliance with environmental regulations.[78] Strategies such as solvent recovery use of water as the reaction medium, and room-temperature synthesis have been proposed, but heir applicability across different MOF and hybrid systems is still limited.[79] Finally, the scale-up of electrode integration for energy storage devices poses additional hurdles. Incorporating MOFs or MOF- derived nanostructures into large area electrodes with mechanical robustness, stable interface and long cycling durability requires innovations in processing methods, binder chemistries, and coating technologies.[80] Without advances in these areas, laboratory- scale performance benchmarks may not translate effectively into commercial supercapacitors or batteries. In summary, addressing these challenges demands a holistic approach that combines synthetic innovation, cost-efficient precursors greener production strategies, and device-level engineering to realize the full potential of MOFs and their hybrids in industrial-scale applications.

3. Applications of MOFs/MXene Composites

View Article Online
DOI: 10.1039/D5CP02795K

MOF/MXene composites offer multifunctional capabilities for environmental remediation through efficient pollutant degradation. The enhanced photocatalytic properties support effective hydrogen (H_2) production via photocatalysis or electrocatalysis. These materials also exhibit high conductivity and stability, ideal for supercapacitor energy storage. Together, they present a sustainable platform for clean energy and environmental technologies. Furthermore, the photocatalytic performance of MXene-based composites is strongly governed by both surface functionalization and morphological control. Functionalization of MXene surface with terminal groups (-O,-OH, -F, -S) or heteroatom doping plays a crucial role in tailoring electronic structures, charge separation efficiency, and interfacial interactions with semiconductors partners. For instance, surface engineering through oxygen rich functionalities enhanced the density of active sites and promotes stronger interactions with co-catalysts leading to improved redox kinetics.[81] Similarly, heteroatom doping (e.g N, S, P) not only improves visible-light absorption but also modulates the band alignment between MXene and semiconductor photocatalyst, thereby facilitating more efficient charge transfer.[82] Morphology control represents another critical factor in optimizing activity. Exfoliation into ultrathin MXene nanosheets or quantum dots significantly enlarges the specific surface area, offering abundant catalytic sites and shortened diffusion pathways for reactants.[71] Hierarchical or three-dimensional MXene architectures have also been demonstrated to mitigate the common issue of nanosheet restacking, ensuring better accessibility of active sites and enhancing light –harvesting efficiency.[73] Moreover, tailoring the lateral size and thickness of MXene sheets directly influence charge carrier mobility and surface reaction kinetics providing an effective way to tune photocatalytic activity toward CO_2 reduction and water splitting.[70] In addition, post-synthetic functionalization with metal cluster or molecular co-catalysts on MXene surface introduces synthetic effects, where MXene act as both electron

View Article Online
DOI: 10.1039/D5CP02795K

mediators and structural scaffolds to stabilize highly dispersed active sites. Such hybridization strategies have been reported to significantly boost photocatalytic efficiency while maintain long term stability under operational conditions.[72] Taken together, surface functionalization and morphology engineering provide powerful levers to tune the photocatalytic activity of MXene-based composites, offering rational design strategies for next-generation catalyst in solar fuel production and environmental remediation.

3.1 Degradation of organic pollutants by MOF/MXene composite;

The degradation of organic pollutants, such as dyes and pharmaceuticals, is a crucial for environmental remediation. MOF/MXene composites have emerged as a promising material for photocatalytic degradation of pollutants due to their high surface area, porosity, and conductivity. The synergy between MOFs and MXene composites enhances the photocatalytic activity, leading to improved degradation efficiency of organic pollutants. MOF/MXene composites have shown potential in degrading complex organic pollutants, such as dyes and pharmaceuticals, under various conditions. The photocatalytic activity of MOF/MXene composites can be tailored by adjusting the composition, structure, and morphology.[83] **Table 2** summarizes the various pollutant degradation using MXene/MOFs composite. Numerous researchers have investigated organic pollutants degradation via MXene/MOF composite. For example, Eslaminejad et al.[59] synthesized palladium nanoparticles supported on MXene/MOF (Pd/MXOF) via a green synthesis route **(Figure 5a)**. The specific surface area of the prepared nanomaterial was 65.874 m^2 g^{-1}. Furthermore, the optical bandgap of the synthesized materials was determined to be 1.79 eV. The prepared nanomaterial was subsequently employed as a visible light-driven photocatalyst for the degradation of Ofloxacin (OFL), as shown in **Figure 5b.** The Pd/MXOF nanomaterial shows complete degradation of OFL after 30 min in the presence of visible light irradiation. In contrast,

View Article Online
DOI: 10.1039/D5CP02795K

the degradation efficiencies of pristine MXene, MOF, and MXOF were 70.8, 57.9, and 37.5%, respectively **(Figure 5c).** In another study**,** Zairov et al.[84] prepared the Neodymium/Dysprosium-based metal organic framework@MXene (Nd/Dy-MOF@MXene) nanocomposite (NC) by the solvothermal method. The bandgap of the prepared composite was 2.78 eV **(Figure 5d)**. The BET surface area was observed to be 55.21 m^2 g^{-1}. The synthesized NC was used to degrade methyl orange (MO) dye **(Figure 5e).** The MO degradation was observed to be 16.23 % in the absence of light. While the MO degradation reached 27.12 %, after light irradiation (without a catalyst). Furthermore, the highest degradation of MO was noted to be 93.55% in the presence of light in 30 min, using Nd/Dy-MOF@MXene as a catalyst **(Figure 5f)**.

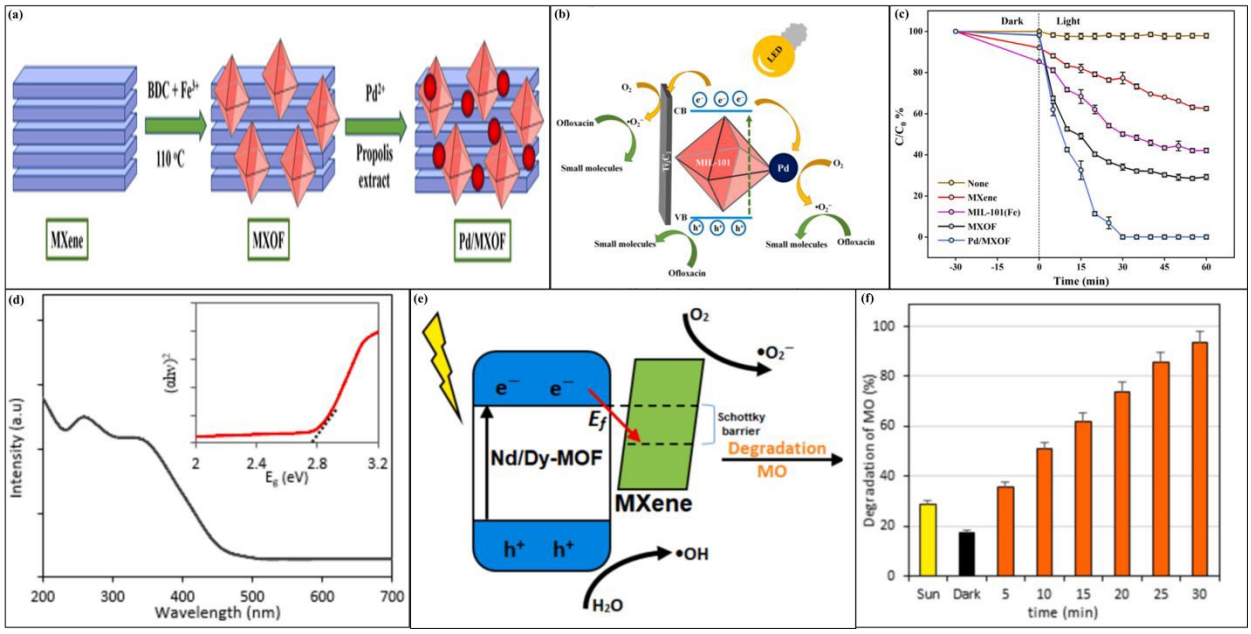

Figure 5. (a) Synthesis of Pd/MXOF nanocomposite, (b) degradation of Ofloxacin (OFL), (c) percent degradation of MXene, MOF, MXOF, and Pd/MXOF. Reproduced with permission from.[59] Copyright 2024, Elsevier, (d) Bandgap of Nd/Dy-MOF@MXene, (e) Mechanism of methyl orange (MO) degradation, and (f) degradation of MO vs time. Reproduced with permission from.[84] Copyright 2025, Elsevier**.**

View Article Online
DOI: 10.1039/D5CP02795K

Similarly, Lin et al.[58] synthesized MX@MCN nanocomposite by solvothermal method. **(Figure 6a)** Surface area and bandgap of the synthesized catalyst were 825 m^2 g^{-1} and 2.4 eV, respectively. **(Figure 6b).** The prepared nanocomposite was used for the photocatalytic activity of Enrofloxacin (ENR) as a catalyst. The (ENR) degradation rate was noted 99 % **(Figure 6c)** at pH 7 **(Figure 6d)** in 60 min, **(Figure 6e)** under visible light irradiation.

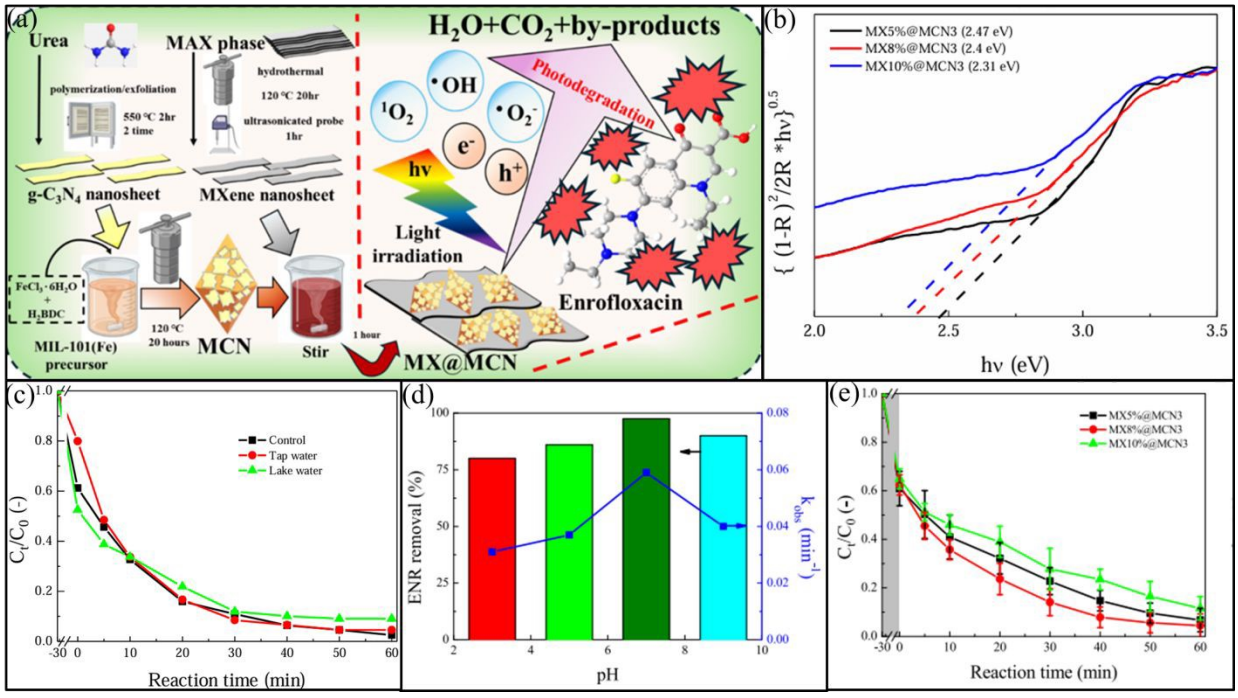

Figure 6. (a) Synthesis of MX@MCN and its photocatalytic activity against enrofloxacin degradation through light (b) bandgap of MX@MCN nanocomposite, (c) Impact of the water matrix on the photodegradation of ENR over MX@MCN photocatalyst when exposed to visible light, (d) pH study of MX@MCN, and (e) photodegradation of enrofloxacin (ENR) over MX@MCN. Reproduced with permission from [58] Copyright 2025, Elsevier**.**

In addition, Wu et al.[85] prepared La-MOF@MXene (LM-0.1) nanocomposite through solvent thermal **(Figure 7a).** The bandgap of the synthesized materials was 1.72 eV. Surface area of the prepared composite was observed to be 58.55 m^2 g^{-1}. **(Figure 7b).** The prepared materials were

View Article Online
DOI: 10.1039/D5CP02795K

used for the photocatalytic degradation of tetracycline HCL. At pH 6 the percent degradation was about 92.4 percent in 120 minutes under the 300 W Xe lamp irradiation **(Figure 7c).** Possible method for degradation TC by LM-0.1 under solar light exposure **(Figure 7d**).

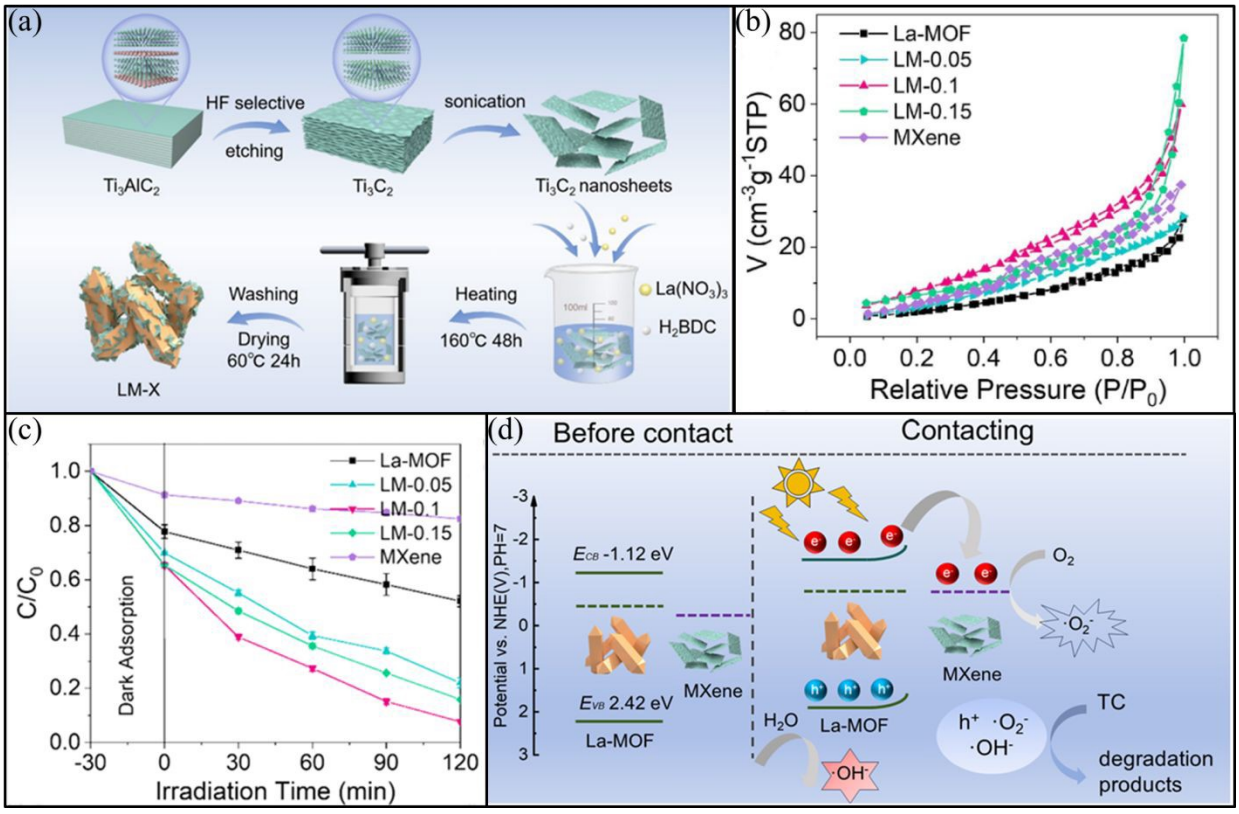

Figure 7. (a) Schematic representation for the preparing of LM-0.1, (b) N_2 adsorption–desorption isotherms, (c) TC removals with xenon lamp and (d) Possible method for degradation TC by LM-0.1 under solar light exposure. Reproduced with permission from [85] Copyright 2025, Elsevier**.**

Furthermore, Tan et al.[86] synthesized DA-M100 nanocomposite by solvent-thermal method. The BET surface area was observed to be 8.8237 $m^2 g^{-1}$. Bandgap of the obtained nanocomposite was calculated to be and 2.93 eV **(Figure 8a).** The prepared nanocomposite was used as a catalyst for the degradation of sulfamethoxazole. The photocatalyst DA-M100 achieves 70 % degradation in

View Article Online
DOI: 10.1039/D5CP02795K

10 minutes and 92.66 % degradation in 60 min at pH 7 **(Figure 8b).** For comparison, the photocatalytic efficiencies of DA-M50, DA-M150 and DA-MIL-88A (Fe) were also studied**.** The removal efficiency of sulfamethoxazole was found to be 93.66%, 87.25% and 89.33% using DA-M50, DA-M150 and DA-MIL-88A (Fe), respectively. The excellent removal efficiency of DA-M100 as compared to DA-M50, DA-M150 and DA-MIL-88A was attributed to their low bandgap**.** The proposed mechanism for the degradation was shown in **(Figure 8c).** The potential photocatalytic activity of DA-M100 under various pH conditions **(Figure 8d).** Similarly, Liu et al.[57] synthesized Ti_3C_2Tx/MIL-53(Fe) (TiCFe) nanocomposite via in-situ method. The prepared nanocomposite was used for the removal of Tetracycline (TC). The prepared photocatalyst showed an excellent removal rate of 90.3 % in 80 minutes due to the xenon lamp as a light source **(Figure 8e)**. The bandgap and surface area of the prepared photocatalyst were 2.10 eV and 17.90 m^2 g^{-1} respectively. The proposed catalytic mechanisms of (TC) were shown in **Figure 8f.**

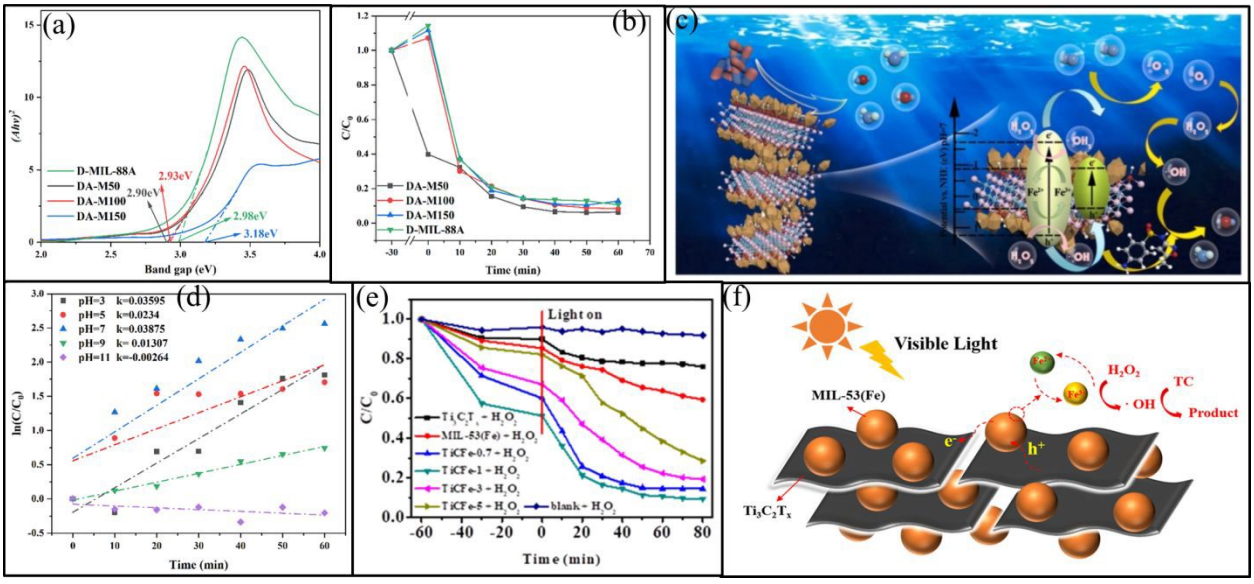

Figure 8. (a) Bandgap of the photocatalysts, (b) SMZ degradation using different photocatalysts (c) schematic representation of DA-M100 adsorption photocatalytic removal method under light

View Article Online
DOI: 10.1039/D5CP02795K

conditions, (d) photocatalytic activity of DA-M100 under different pH conditions. Reproduced with permission from.[86] Copyright 2023, Elsevier**.** (e) Photocatalytic reduction of the Tetracycline employing different photocatalysts after 80 min of visible light and (f) Schematic representation to degrade TC over TiCFe-1 composite under visible light. Reproduced with permission from.[57] Copyright 2020, Elsevier.

Cao et al.[62] prepared the photocatalyst Sn–Bi–MOF/Ti_3C_2 through the solvothermal method. The synthesized catalyst was used to degrade tetracycline (TC). The (TC) degrade only 9.9 % when there is no catalyst present. The degradation efficiency of Sn–Bi–MOF and Ti_3C_2 after 90 minutes of photocatalysis, were 79.7 %, and 69.1% and respectively **(Figure 9a).** After doping Ti_3C_2 to Sn–Bi–MOF, the degradation of (TC) reached to 96.2 % at pH 11 in the presence of a xenon lamp as a light source **(Figure 9b)**. The surface area and bandgap were 145.873 m^2 g^{-1} and 3.02 eV respectively. The proposed photocatalytic mechanism of Sn–Bi–MOF/Ti_3C_2 **(Figure 9c) .**[87] In addition, Cheng et al.[62] synthesized UNiMOF/Ti_3C_2 photocatalyst by the electrostatic self-assembly process **(Figure 9d).** The synthesized materials were used to degrade the methylene blue (MB) dye. The percentage degradation of the synthesized catalyst has an excellent efficiency of 99.49 % in 120 minutes at pH 6.8 in the presence of a xenon lamp as a light source. The degradation efficiency of (MB) at different catalysts **(Figure 9e).** The synthesized photocatalyst has bandgap and surface area of 3.43 eV and 27.00 m^2 g^{-1} respectively. The photocatalytic mechanism of UNiMOF towards methylene blue (MB), **(Figure 9f**).

View Article Online
DOI: 10.1039/D5CP02795K

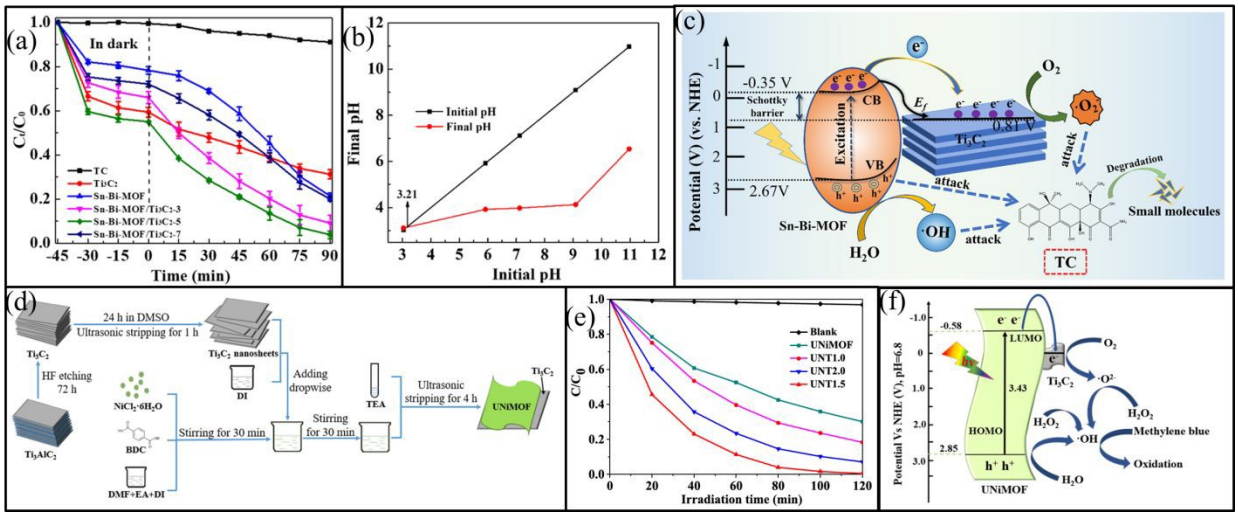

Figure 9. (a) Tetracycline (TC) degradation of Sn–Bi–MOF/Ti_3C_2, (b) pH effects of Sn–Bi–MOF/Ti_3C_2 on TC, and (c) suggested photocatalytic mechanism of Sn–Bi–MOF/Ti_3C_2 Reproduced with permission from.[87] Copyright 2023, Elsevier. (d) Fabrication procedure of the UNiMOF/Ti_3C_2 composites, (e) Degradation of MB over the UNiMOF, Ti_3C_2 and UNiMOF/Ti_3C_2 nanocomposite, and (f) the photocatalytic mechanism of UNiMOF towards (MB). Reproduced with permission from.[62] Copyright 2021, Elsevier.

Far et al.[68] prepared MXene@UiO-66 nanocomposite through a solvothermal in situ growth method **(Figure 10a).** The synthesized nanocomposite was utilized for the degradation of (MB) and direct red 31 (DR31). The surface area and bandgap of the prepared nanocomposite were 347.28 m^2 g^{-1} and 4.04, respectively **(Figure 10b)**. In the presence of Mercury Vapor (250W) as a light source, the degradation efficiency of (MB) **(Figure 10c).** And direct red 31 (DR31) **(Figure 10d),** was 78 % and 56 % within 60 minutes, respectively.The proposed mechanism of photodegradation **(Figure 10e)**.

View Article Online
DOI: 10.1039/D5CP02795K

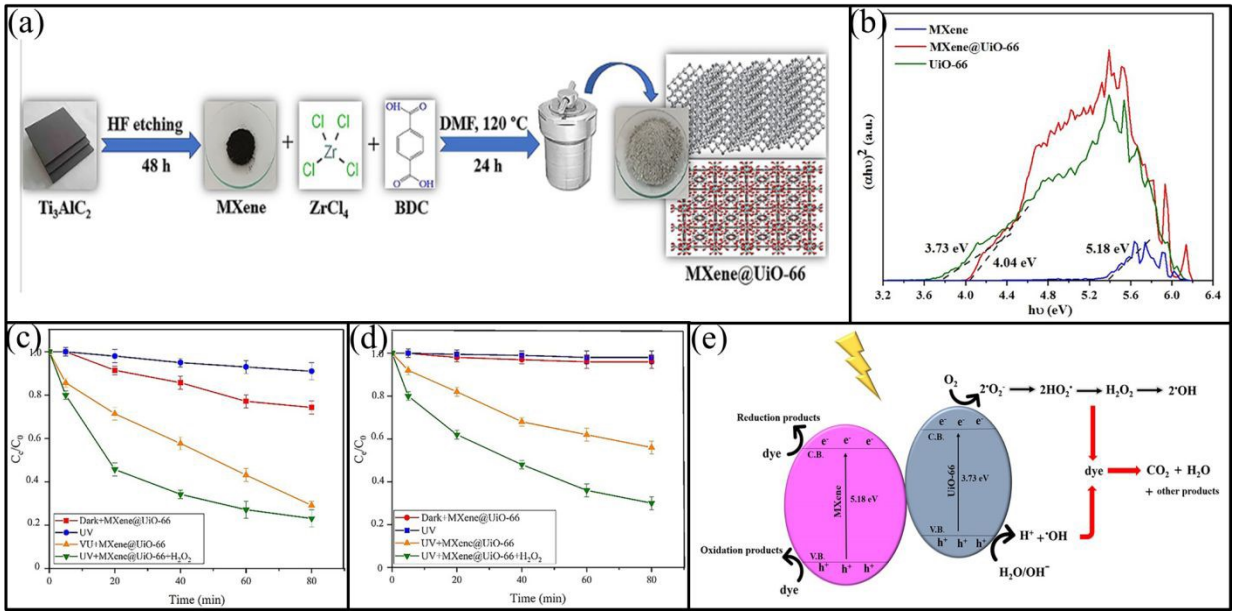

Figure 10. (a) Schematic representation for the synthesis of MXene@UiO-66 nanocomposite, (b) bandgap of MXene, UiO-66, MXene@UiO-66, (c) Degradation performance of MXene@UiO-66 nanocomposite with (MB), (d) degradation of direct red 31 (DR31), and (e) Schematic representation of MB and DR31 degradation mechanism using MXene@UiO-66 composite. Reproduced with permission from.[68] Copyright 2024, Elsevier.

Table 2. Summary of the photo-catalytic degradation of organic pollutants by MOF/MXene based composite.

Pollutant	photocatalyst	Synthesis method	Catalyst properties		Concentration		Reaction conditions			Removal (%)	Rate constant (min^{-1})	Reference
			Band gap (eV)	Surface area (m^2/g)	Pollutant conc. (mg/L)	Catalyst dose (mg/L)	Light source	Time (min)	pH	.		
Ciprofloxacin	VCo-MOF@$Ti_3C_2T_x$	Solvothermal	---	150.72	20	5 mg	---	30	5.5	96.1	0.061	[88]
Ofloxacin (OFL)	Pd/MXOF	green approach	1.79	65.874	20	0.4	Visible light	30	5.0	100	---	[59]
Sulfamethoxazole	DA-M100	Solvothermal	2.93	8.8237	20	50 mg	Xenon lamp	60	7.0	92.6	---	[86]
Tetracycline hydrochloride	La-MOF@MXene (LM -0.1)	solvent thermal	1.72	58.55	10	10 mg	300 W xenon lamp	120	6.0	92.4	0.00773 min^{-1}	[85]
Enrofloxacin (ENR)	MX@MCN	thermal solvent	2.4	825	10	0.25g/L	Visible light	60	7.0	99.0	0.069 min^{-1}	[58]
Tetracycline (TC)	TiCFe	Solvothermal	2.10	17.90	10	10 mg	Xenon lamp	80	---	90.3	0.0286 min^{-1}	[57]
Tetracycline (TC)	Sn–Bi–MOF/Ti_3C_2	Solvothermal	3.02	145.873	20	40	Xenon lamp	90	11.0	96.2	---	[87]
methylene blue (MB)	MXene@UiO-66	Solvothermal in situ growth method	4.04	347.28	20	10 mg	Mercury Vapor (250W)	60	---	78.0	---	[68]

direct red 31 (DR31)	MXene@UiO-66	Solvothermal in situ growth method	4.04	347.28	20	10 mg	Mercury Vapor (250W)	60	---	56.0	---	[68]
Methylene blue (MB)	UNiMOF/Ti_3C_2	Electrostatic self-assembly process	3.43	27.00	20	50 mg	Xenon lamp	120	6.8	99.49	2.4822 h^{-1}	[62]
methyl orange dye	Nd/Dy-MOF@MXene	Solvothermal	2.78	55.21	10	20 mg	Sunlight	30	3.0	93.55	0.0989 min^{-1}	[84]
Acetone (C_3H_6O)	MXene/MOF aerogel MPA-m/U66N-M	Hydrothermal	2.40	1205	200	0.1 g	Xenon lamp	60	---	95.0	0.052 min^{-1}	[53]
Methylene blue (MB)	MXOF	via in-situ growth	4.99	850.86	20	30 mg	Mercury Vapor	60	---	62.0	0.0142 min^{-1}	[69]
tetracycline (TC)	BOC/Ti_3C_2	Hydrothermal	2.64	---	20	55 mg	Xenon lamp	120	5.5	81.0	0.05223 $mg^{-1}\cdot L\cdot min^{-1}$	[89]

tetracycline hydrochloride	NH2-MIL-125(Ti)(TiO_2)/Ti_3C2 (MT5)	one step solvothermal strategy	---	329	20	0.2g/L	Xenon lamp	60	10.5	82.8	0.034 min^{-1}	[51]
tetracycline	Ti-MOF/QDs/ZIS	electrostatic attraction method	2.16	179.8	20	15 mg	Xenon lamp	50	---	96.0	0.0487 min^{-1}	[63]
sulfamethazine	Ti-MOF/QDs/ZIS	electrostatic attraction method	2.16	179.8	30	15 mg	Xenon lamp	40	---	98.0	0.0487 min^{-1}	[63]
Cr(VI)	Ti_3C_2/UiO-66-NH_2	In-situ growth	..	..	100	10 mg	Xenon lamp	40	2.0	100.0	0.0871 min^{-1}	[67]

View Article Online
DOI: 10.1039/D5CP02795K

3.1.1 Mechanisms of degradation by MOF/MXene composite;

The photocatalytic degradation of organic contaminants using MOF/MXene composites is illustrated in **Figure 11a.** Photocatalytic studies have shown that MOF/MXene composite absorbs light and energy, resulting in the excitation of electrons and the formation of electron-hole pairs.[90, 91] The migration of excited electrons through the conduction bands of MOFs and MXene suppresses electron-hole recombination, thereby enhancing radicals' generation and improving photodegradation efficiency. The generation of reactive radicals primarily depends on the presence of photoexcited electrons and holes. Specifically, when the photoinduced holes (h^+) interact with water molecules, produce proton and hydroxyl radicals, while concurrently converting molecular oxygen into superoxide radicals. The superoxide radicals then react with protons to form hydroperoxyl radicals, which under specific conditions lead to the formation of hydrogen peroxide. Subsequently, Hydrogen peroxide decomposes to release additional molecular oxygen and generate more hydroxyl radicals (•OH), enhancing the oxidative environment. The self-propagating cycle amplifies radical concentration, thereby enabling the degradation of dye molecules into non-toxic byproducts.[83] The electron transport mechanism within the Sn–Bi–MOF/Ti_3C_2 heterostructure is well-aligned with the principles of a Schottky junction. Ti_3C_2 acting as a conductive substrate forms a Schottky barrier at its interface with semiconductors.[92] Upon illumination, electrons in the valence band of the Sn–Bi–MOF catalyst become photoexcited to the conduction band, leaving (h^+) in the valence band. The high conductivity of Ti3C2 facilitates the rapid migration of electrons from the band of Sn–Bi–MOF conduction band to its own structure. Over time, the accumulation of electrons in Ti_3C_2 and holes in the valence band of Sn–Bi–MOF leads to the formation of a space-charge layer at the interface, constituting a Schottky barrier that effectively traps electrons and prevents their recombination.[93] This mechanism

View Article Online
DOI: 10.1039/D5CP02795K

significantly extends the lifetime of photogenerated charge carriers. Simultaneously, electrons on the Ti_3C_2 surface react with oxygen molecules in the electrolyte to generate superoxide radicals ($O_2^{\bullet-}$), while the holes in the Sn-Bi-MOF valence band oxidize water to form hydroxyl radicals (•OH), both of which contribute to the degradation of tetracycline (TC) into smaller, less harmful molecules. The suggested photocatalytic mechanisms of the Sn–Bi–MOF/Ti_3C_2 system, as depicted in **Figure 11b.** Upon light radiation, the semiconductor photocatalyst (Sc) absorbs photons with energy equal to or greater than its bandgap, promoting electrons from the valence band (VB) to the conduction band (CB), and generating holes in the VB **(equation 1).** These photogenerated holes oxidize water molecules adsorbed on the catalyst surface, producing reactive hydroxyl radicals (•OH) and protons **(equation 2)**. In addition, hydrogen peroxide present in the reaction can accept conduction band electrons, producing hydroxyl radicals and hydroxide ions **(equation 3).** Photogenerated holes may also oxidize surface hydroxyl ions, further contributing to hydroxyl radicals' generation **(equation 4).** Meanwhile, dissolved oxygen molecules capture conduction band electrons to form the superoxide anion radicals ($O_2^{\cdot-}$) **(equation 5).** These superoxide radicals subsequently react with protons to form hydroperoxyl radicals (·OOH) **(equation 6).** Hydroperoxyl radicals can further react with each other to yield hydrogen peroxide and molecular oxygen **(equation 7).** Finally, the reactive oxygen species (·OH, $O_2^{\cdot-}$, ·OOH) and photogenerated holes degrade organic contaminants into harmless mineralized products like carbon dioxide and water **(equation 8).**[94]

$$Sc + h\upsilon \rightarrow h^+_{VB} + e^-_{CB} \quad (1)$$

$$H_2O + h^+_{VB} \rightarrow {}^{\bullet}OH + H^+ \quad (2)$$

$$H_2O_2 + e^-_{CB} \rightarrow {}^{\bullet}OH + OH^- \quad (3)$$

View Article Online
DOI: 10.1039/D5CP02795K

$OH^- + h+ VB \rightarrow {}^{\bullet}OH$ (4)

$O_2 + e{-}CB \rightarrow O_2^{\bullet -}$ (5)

$O_2^{\bullet -} + H+ \rightarrow {}^{\bullet}OOH$ (6)

$2{}^{\bullet}OOH \rightarrow H_2O_2 + O_2$ (7)

${}^{\bullet}OH/O_2^{\bullet -}/h^+ + \text{organic pollutants} \rightarrow \text{degradation products} + CO_2 + H_2O$ (8)

When irradiated with light, the MXene@UiO-66 nanocomposite generates electron-hole pairs, with an electron in the CB and a hole in the VB. Electrons excited in the CB of MXene can transfer to the CB of UiO-66 due to their favorable alignment. Additionally, holes are transferred from the VB of UiO-66's to the VB of MXene's due to higher CB edge potential of MXene relative to UiO-66's.[95] Water molecules present in the DR31and MB dye solutions can be oxidized via photogenerated species in the CB to produce ${}^{\bullet}OH$. Additionally, CB electrons can reduce ambient oxygen to produce superoxide radicals (O_2^-**)**. These reactive species, including superoxide radicals and hydroxyl radicals, synergistically degrade the MB and DR31 dye molecules into smaller, less harmful compounds [96]. The internal electric field formed at the MXene -UiO-66 interface, coupled with charge carrier cycling, effectively suppresses the recombination of photogenerated electron-hole pairs. As a result, the overall photocatalytic degradation efficiency of the MXene@UiO-66 nanocomposite is significantly enhanced. The proposed photocatalytic degradation mechanism facilitated by MXene@UiO-66 is illustrated in **Figure 11c.**

View Article Online
DOI: 10.1039/D5CP02795K

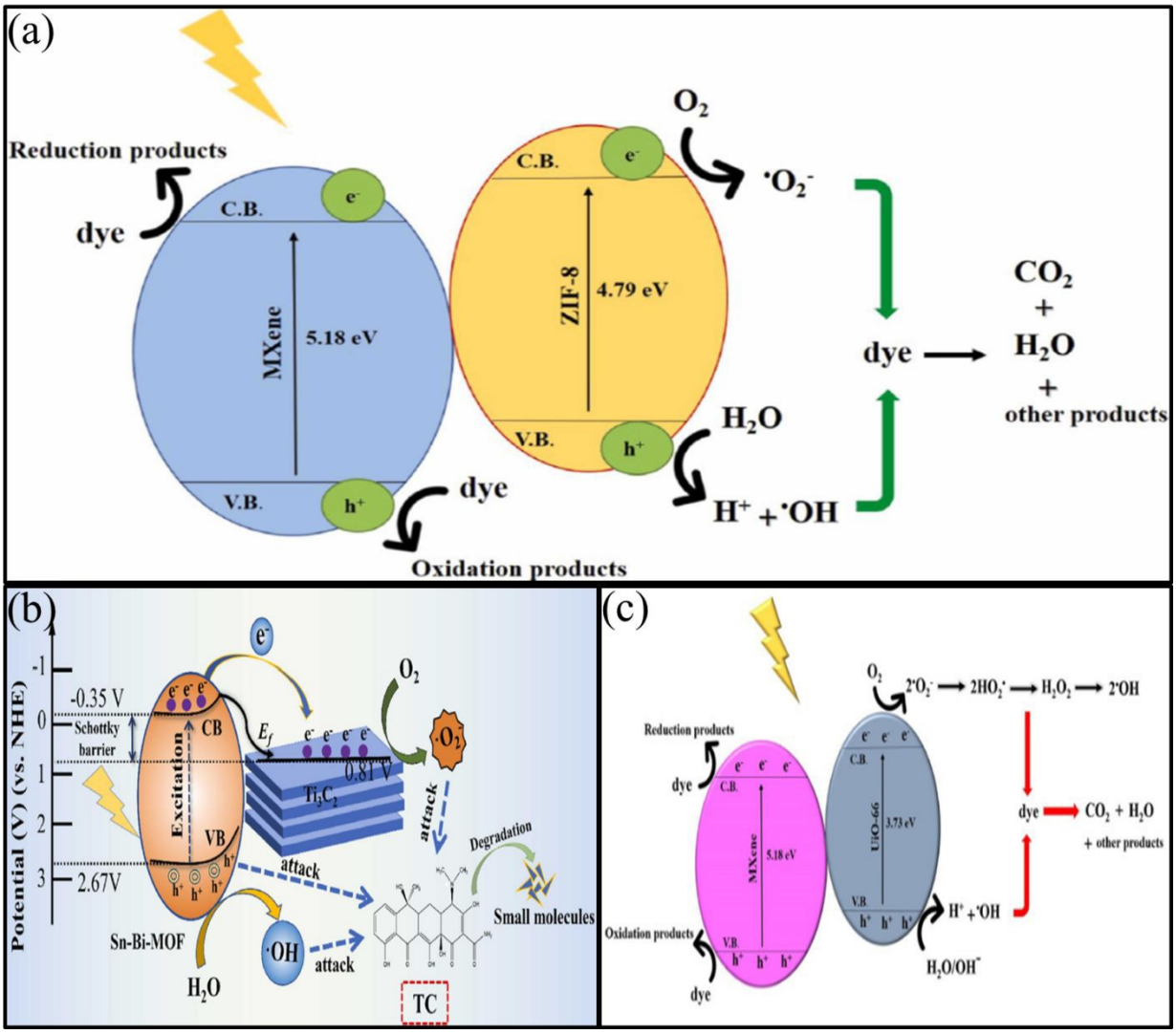

Figure 11. (a) The degradation method by the MXOF nanocomposite. Reproduced with permission from.[69] Copyright 2023, Elsevier. (b) The suggested photocatalytic mechanism in Sn–Bi–MOF/Ti_3C_2.[87] (c) Schematic representation of MB and DR31 degradation mechanism using MXene@UiO-66 nanocomposite. Reproduced with permission from.[68] Copyright 2024, Elsevier.

View Article Online
DOI: 10.1039/D5CP02795K

3.2 Hydrogen production by MOF/MXene composite;

Hydrogen can be used as a clean energy carrier, offering a potential alternative to fossil fuels and reducing greenhouse gas emissions. Hydrogen production through photocatalytic water splitting is a promising approach for producing clean and sustainable energy. MOF/MXene composites have emerged as promising materials for photocatalytic hydrogen production due to their enhanced charge separation and improved light absorption.[97] The combination of MOFs and MXene optimizes the electronic structure, reducing kinetic energy barriers and improving catalytic performance.[98] The experimental studies have demonstrated the superior hydrogen evolution performance of MOF/MXene composites, the underlying atomic-level origin of this activity require further clarification. Recent density functional theory (DFT) investigations provide valuable mechanistic insights into how interfacial electronic interactions dictate catalytic efficiency. The intimate electronic coupling at MOF/MXene interface plays a decisive role in regulating efficiency for hydrogen evolution, and density functional theory (DFT) calculations have been instrumental in clarifying the underlying atomic-level processes. Recent work on 2D MOF-$Ti_3C_2T_x$ Schottky-type heterojunctions revealed strong interfacial charge redistribution, rate of photogenerated carriers and simultaneously shift the metal-center d-band toward optimal H^+ binding [99]**.** In Ni-MOF/g-C_3N_4/Ti_3C_2 hybrids, DFT showed that electrons preferentially flow from MXene into Ni nodes, thereby reducing ΔG- H^+ and creating a thermodynamically more favorable landscape for the Volmer stem.[100] Beyond charge transfer, interfacial coordination and defect chemistry introduce additional active motifs. Coordination bonding between MXene surface terminations (-O, -OH) and MOF secondary building units generates low-coordination metal centers that exhibit near-thermoneutral adsorption energies for H^+, providing kinetically accessible pathways for both Volmer and Heyrovsky/Tafel processes.[101] Similarly, bimetallic MOF/MXene

View Article Online
DOI: 10.1039/D5CP02795K

composites, such as MIL-100ZIF-7/MXene, display enhanced stabilization of reaction intermediates due to interfacial electronic synergy; a conclusion reinforced by both experimental HER activity and supporting DFT calculation.[102] Complementary reviews also highlight that Schottky-junction behavior, widely observed in MOF/MXene heterostructues, establishes internal fields that direct charge flow across the interface and prolong, carrier lifetime, ultimately enhancing hydrogen evolution efficiency.[103] Collectively, these computational studies converge on a unifying mechanism: (i) directional charge transfer at the MOF/MXene interface modulates the electronic structure of catalytic sites, (ii) defect and coordination-driven low-coordination metal centers offer optimized hydrogen adsorption, and (iii) Schottky-type alignment suppresses recombination and accelerates proton-electron coupling. These atomic-level insights explain the superior hydrogen evolution performance consistently observed in MOF/MXene hybrids and highlight the importance of rational interfacial engineering guided by theory. Summary of photocatalytic hydrogen production long with other parameters are presented in **Table 3**. Many researchers have studied the hydrogen production using MXene/MOF composites. For example, Li et al.[104] synthesized Ti_3C_2@MIL-NH_2 nanocomposite **(Figure 12a).** The BET surface area of the prepared catalyst was 69.2 m^2 g^{-1}. The bandgap of the synthesized materials was 2.40 eV. The prepared nanocomposite was utilized as a catalyst for hydrogen production. The Ti_3C_2@MIL-NH_2 showed the hydrogen evolution activity of 4383.1 μmol/h/g **(Figure 12b),** with an apparent quantum yield of 3.140%, which was 6 times higher, and 5 times higher than that shown by pristine MIL-NH2 and the physical mixture of MIL-NH_2 and Ti_3C_2. The Ti_3C_2@MIL-NH_2 showed higher efficiency due the presence of Ti_3C_2. It is due to the fact that Ti_3C_2 enhances the charge carrier mobility and separation, thereby reducing the charge carrier recombination rate. The proposed mechanisms was given in **(Figure 12c).**

View Article Online
DOI: 10.1039/D5CP02795K

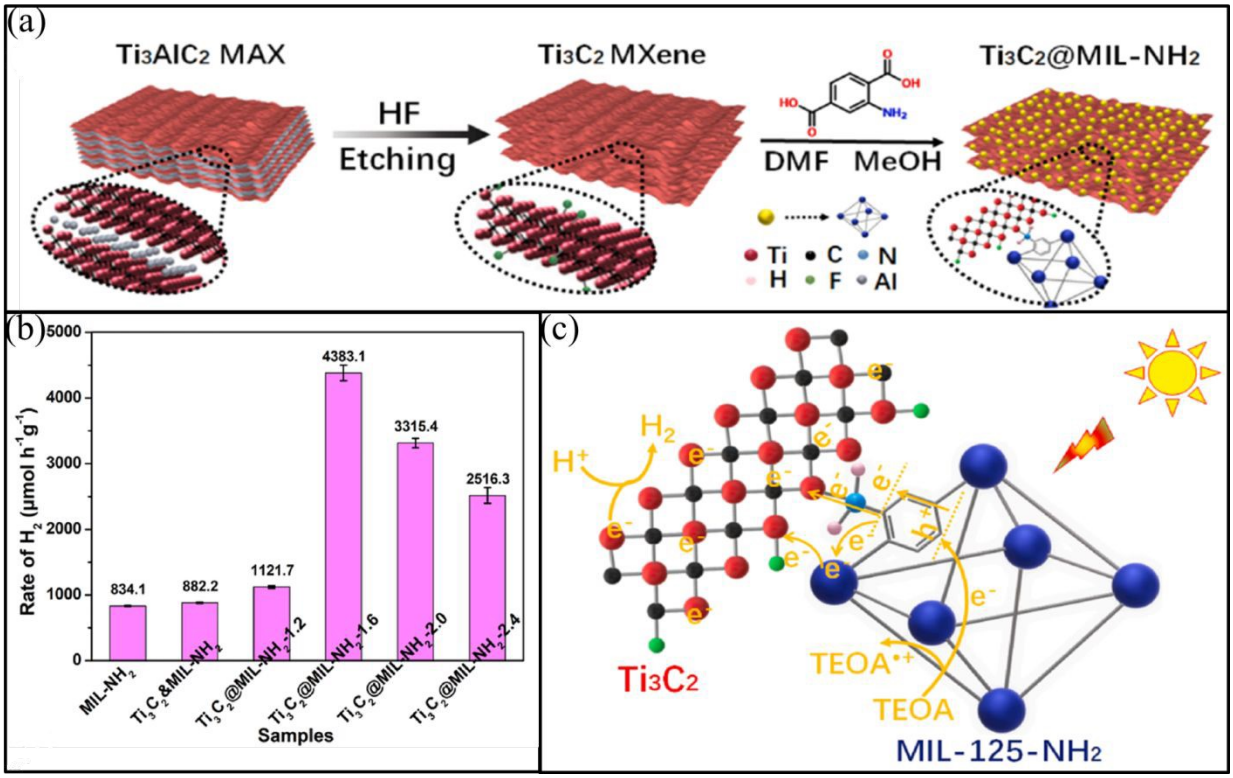

Figure 12. (a) Schematic preparation process of Ti_3C_2@MIL-NH_2, (b) H_2 production over MIL-NH_2, Ti_3C_2&MIL-NH_2 and Ti_3C_2@MIL-NH_2 composites, and (c) Mechanism for H_2 production over the Ti_3C_2@MIL-NH_2 composite. Reproduced with permission from.[104] Copyright 2021, Elsevier.

Rajan et al.[101] prepared Ni-MOF/CN/TC catalyst for hydrogen production. The bandgap of the synthesized catalyst was 2.1 eV. Ni-MOF/CN/TC catalyst produce 1044.46 µmol/g hydrogen at pH 11 in the presence solar light (1.5AM_0) using TEOA as sacrificial agent. Ti_3C_2 (TC) was used as a co-catalyst. The TC have different weight % which were 4, 8, and 12, which were labeled as 15Ni-MOF/CN/4TC, 15Ni-MOF/CN/8TC and 15Ni-MOF/CN/12TC, respectively. The hydrogen generation was determined to be 800.54 µmol/g, 1044.46 µmol/g and 910.25 µmol/g, for 15Ni-

View Article Online
DOI: 10.1039/D5CP02795K

MOF/CN/4TC, 15Ni-MOF/CN/8TC and 15Ni-MOF/CN/12TC, respectively. However, despite having high concentration of TC, the 15Ni-MOF/CN/12TC have shown lower hydrogen production rate because higher concentration of TC occupied active site of 15Ni-MOF as well as they shield incident light. The sacrificial agent in the production of hydrogen was TEOA. Similarly, Shi et al. (2022) synthesized UZT/CFMX nanocomposite as a photocatalyst for hydrogen production **(Figure 13a).** The surface area of the prepared composite was calculated to be 371.9 m^2 g^{-1}. The bandgap of the prepared nanocomposite was 2.82 eV **(Figure 13b).** The UZT/CFMX showed the hydrogen production rate of 2187 µmol/g/h, which was 20 times greater than pristine UZT and four times higher than UZT/MX **(Figure 13c).** The mechanisms of the UZT/CFMX for hydrogen production were in **(Figure 13d)**.

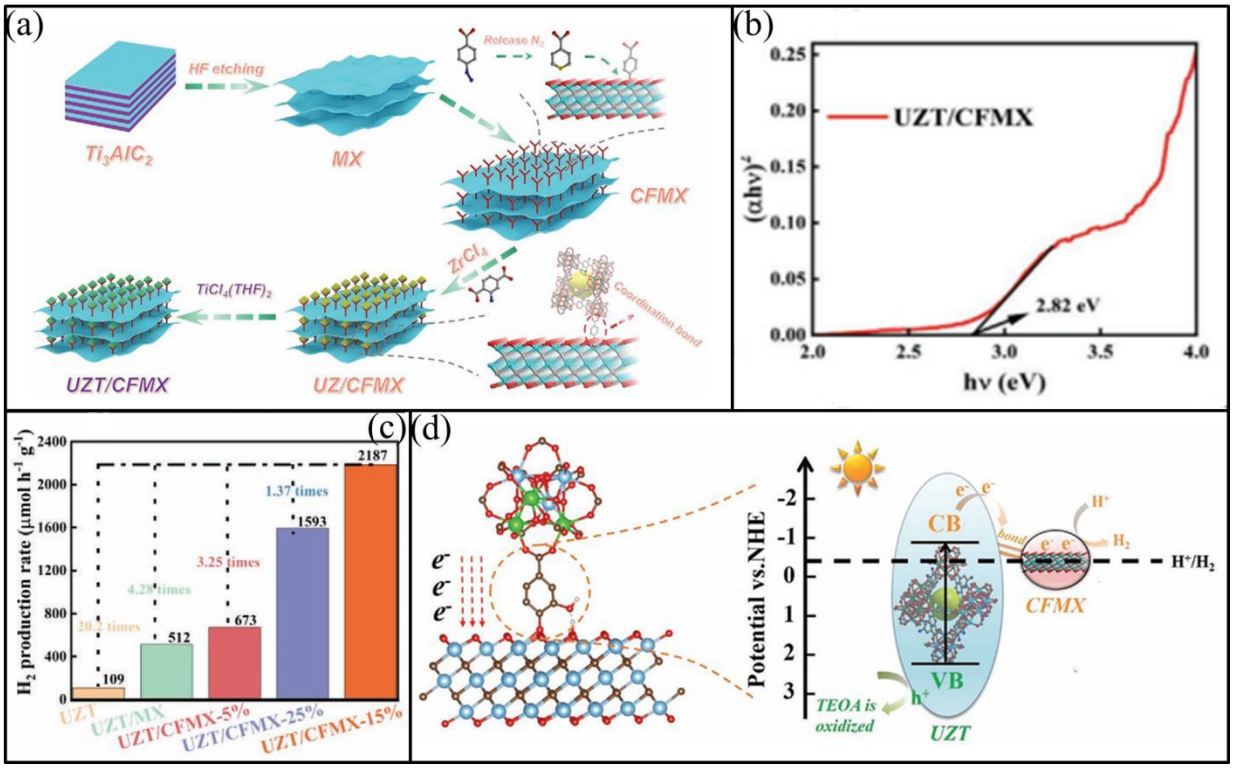

Figure 13. (a) Schematic illustration for constructing the UZT/CFMX heterostructure (b) Bandgap of UZT/CFMX, (c) H_2 production of UZT, UZT/MX, UZT/CFMX-5%, UZT/CFMX-15%, and

View Article Online
DOI: 10.1039/D5CP02795K

UZT/CFMX-25%, and (d) Photocatalytic water splitting mechanism for UZT/CFMX. Reproduced with permission from.[101] Copyright 2022, open access CC BY 4.0.

Sun et al.[105] prepared Co-ZIF-9/Ti_3C_2 nanocomposite as a photocatalyst for hydrogen production **(Figure 14a).** 53.0 m^2 g^{-1} was the surface area of the synthesized photocatalyst. The Co-ZIF-9/Ti_3C_2 had hydrogen production rate was 3538.5 μmol/g/h. The Co-ZIF-9/Ti_3C_2 was synthesized with various weight % of Ti3C2, i.e., 2.0 wt%, 2.5 wt%, and 3.0 wt% which was denoted as CZT2.0, CZT2.5 and CZT3.0, respectively. CZT2.5 had the highest hydrogen production which was (3538.5 μmol/g/h), which was 9.6 times as high as that of pristine Co-ZIF-9. The Co-ZIF-9 have low photocatalytic activity of (356.0 μmol/g/h), because of the quick recombination of electron hole. Hydrogen production rate of different catalyst was given in **(Figure 14b).** The apparent quantum yield of the prepared photocatalyst was 4.8 % at 420 nm. The sacrificial agent was Na_2S (0.1 M)/Na_2SO_3 (0.5M). 300 W xenon lamp was the light source. Mechanism for H_2-production over the Co ZIF-9/Ti_3C_2 composite **(Figure 14c)**.

View Article Online
DOI: 10.1039/D5CP02795K

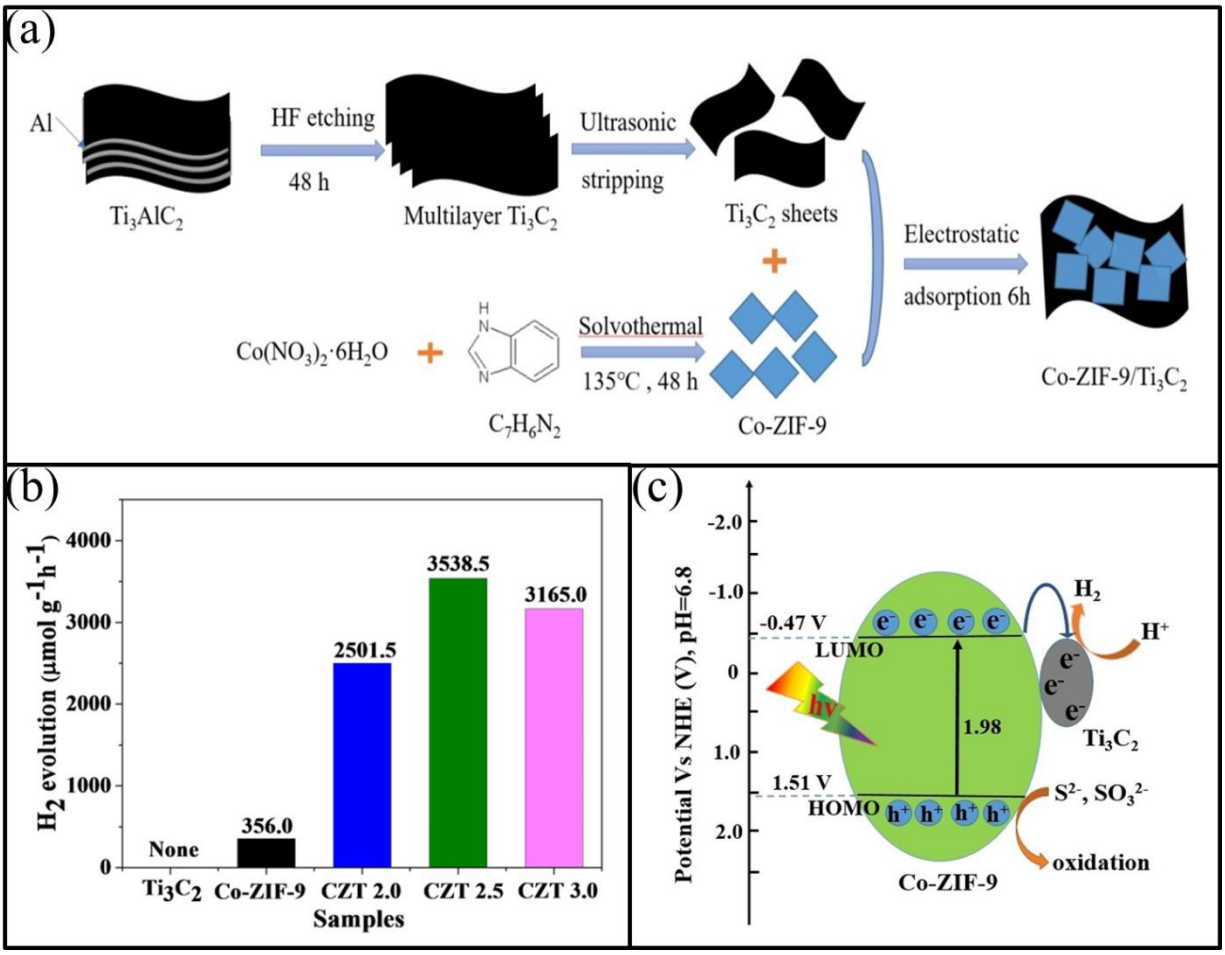

Figure 14. (a) Synthesis of Co-ZIF-9/Ti_3C_2, (b) comparison of H_2- production rate over different samples, and (d) Mechanism for H_2-evolution over the Co-ZIF-9/Ti_3C_2. Reproduced with permission from.[105] Copyright 2022.

Tian et al.[52] synthesized Ti_3C_2/TiO_2/UiO-66-NH_2 nanocomposite as photocatalysts for hydrogen production **(Figure 15a).** The prepared photocatalysts have the surface area and bandgap 987.5 m^2 g^{-1} and 2.75 eV, respectively **(Figure 15b).** The prepared photocatalysts was utilized for hydrogen generation. Ti_3C_2/TiO_2/UiO-66-NH_2 had the hydrogen evolution activity of 1980 μmol/h/g which was about 2.5 times and 1.5 times higher than that of UiO-66-NH_2 and Ti_3C_2Tx/UiO-66-NH_2 respectively. The hydrogen production rate of different materials were given in **(Figure 15c).** The

View Article Online
DOI: 10.1039/D5CP02795K

hydrogen production rate increases by the addition of TCA (co-catalysts). The proposed mechanisms for hydrogen production were given in the **(Figure 15d).**

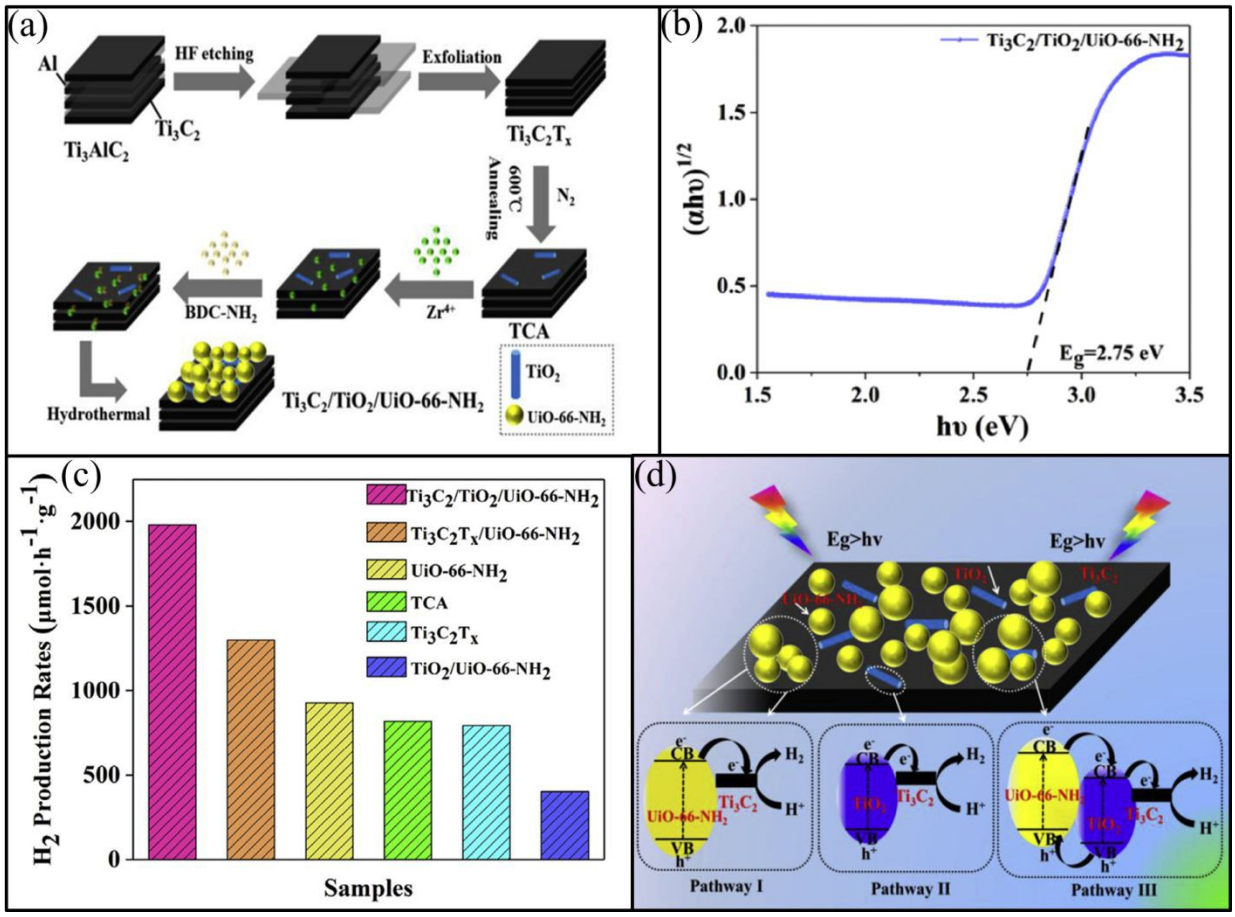

Figure 15. (a) Diagrammatic representation of a possible chemical route for the synthesis of $Ti_3C_2/TiO_2/UiO\text{-}66\text{-}NH_2$, (b) Bandgap for $Ti_3C_2/TiO_2/UiO\text{-}66\ NH_2$ nanocomposite, (c) The as prepared samples had average H_2 production, and (d) Charge-transfer paths for $Ti_3C_2/TiO_2/UiO\text{-}66\text{-}NH_2$ are shown schematically. Reproduced with permission from.[52] Copyright 2019, Elsevier.

Table 3. Summary of the photo-catalytic hydrogen production

Catalyst	Co-catalyst	Bandgap (eV)	Surface area (m^2/g)	Reaction Conditions			Sacrificial agents	Hydrogen Production ($\mu mol\ g^{-1}\ h^{-1}$)	Apparent quantum yield (AQY)	Reference
				Catalyst dosage (mg)	Light Source	Time (min)				
Ti_3C_2@ MIL-NH_2	Ti_3C_2	2.40	69.2	70	300 W Xenon arc lamp	180	0.3 mL TEOA	4383.1	3.140%	[104]
Co-ZIF-9/Ti_3C_2	---	---	53.0	50	300 W Xenon lamp	---	Na_2S (0.1 M)/Na_2SO_3 (0.5M)	3538.5	4.8% 420 nm	[105]
UZT/CFMX	MX or CFMX	2.82	371.9	---	Xenon lamp	---	TEOA	2187	---	[101]
Ti-MOF/QDs/ZIS	---	2.16	179.8	25	Xenon lamp	---	0.35 M Na_2S and 0.25 M Na_2SO_3	2931.9	---	[63]
TiO_2-Ti_3C_2-CoS_x	CoS_x and Ti3C2	---	---	20	300 W Xenon lamp	---	Methanol	950	---	[106]
Ti_3C_2/TiO_2/UiO-66-NH_2	TCA	2.75	987.5	20	300W Xenon lamp	--	0.1 M Na_2S and 0.1 M Na_2SO_3	1980	---	[52]
TT/CuTMOF	---	1.74	---	10	300W Xenon lamp	360	TEOA	19,060	---	[107]

Ti_3C_2/UiO-66-NH_2 (TU10)	---	2.67	984	20	350 W Xenon lamp	---	0.1 M Na_2S and 0.1 M Na_2SO_3	204	---	54
Ni-MOF/CN/TC	Ti_3C_2 (TC)	2.1	---	5	Solar light ($1.5AM_0$)	3 h	TEOA	1044.46	---	100
TiO_2/Ti_3C_2–TiC/CZUNH	---	---	348.29	---	Visible light	60 min	methanol	570	---	108
TCs/Cu-PMOF	---	1.73	20.3	10	300 W Xenon lamp	360	triethanolamine	1690	---	109

View Article Online
DOI: 10.1039/D5CP02795K

3.2.1 Mechanisms of hydrogen production by MOF/MXene composite;

The photocatalytic water splitting process, can be divided into two main stages: PEC (photo-electrochemical) and photocatalytic reactions.[110] In particular the PEC process utilizes light energy to initiate a chemical reaction that results in hydrogen (H_2) production. During this process, a semiconductor material is typically submerged in an electrolyte solution to enable the reaction. Upon exposure to light, the semiconductor absorbs photons, initiating the generation of electron-hole pairs. These excited charge carriers are then separated by internal electric field or an externally applied bias a phenomenon known as charge separation. Next in a redox mechanism, the excited electrons migrate to the cathode (also known as the photocathode) whereas they reduce water molecules to form hydrogen gas. Simultaneously, the photo-generated holes move to the photoanode, where they oxidize water to generate oxygen. These electrons flow through an external circuit from the photoanode to the photocathode, completing the circuit in a process called electron transfer. This led to the final stage known as gas evolution, where hydrogen is released at the cathode and oxygen at the anode. When light with energy exceeding the semiconductor band gap strikes the photoanode, electrons are excited into conduction band (CB), while holes remain in the valence band (VB). These photogenerated electrons travel through the external circuit to reach the cathode, facilitated by the potential difference across the photoanode. At the cathode, protons (H^+) in the solution are reduced to form hydrogen gas.[111] A possible mechanism for photocatalytic hydrogen production is illustrated in the **(Figure 16).** In this mechanism, light energy excites the semiconductor (SC) producing an electron-hole pair **(equation 9).** The hole participates in oxidizing water molecules, producing protons and releasing oxygen gas **(equation 10).** This oxidation reaction is crucial part of the overall water splitting process, which releases electrons, protons, and oxygen **(equation 11).** Finally, the generated electrons reduce protons to

View Article Online
DOI: 10.1039/D5CP02795K

produce molecular hydrogen **(equation 12).** Overall, the water splitting reaction yields hydrogen and oxygen gases, requiring an energy input of 237 kJ/mol of energy (overall reaction) **(reaction 13)**.[94]

Light absorption: $sc + hv \rightarrow e^- + h^+$ (9)

Oxidation of water: $4\,h^+ + 2H_2O \rightarrow 4H^+ + O_2$ (10)

Water splitting reaction: $2H_2O \rightarrow O_2 + 4H^+ + 4e^-$ (11)

Reduction of protons: $4H^+ + 4e^- \rightarrow 2H_2$ (12)

Overall water splitting: $2H_2O \rightarrow 2H_2 + O_2\ \Delta G = 237$ kJ/mol (13)

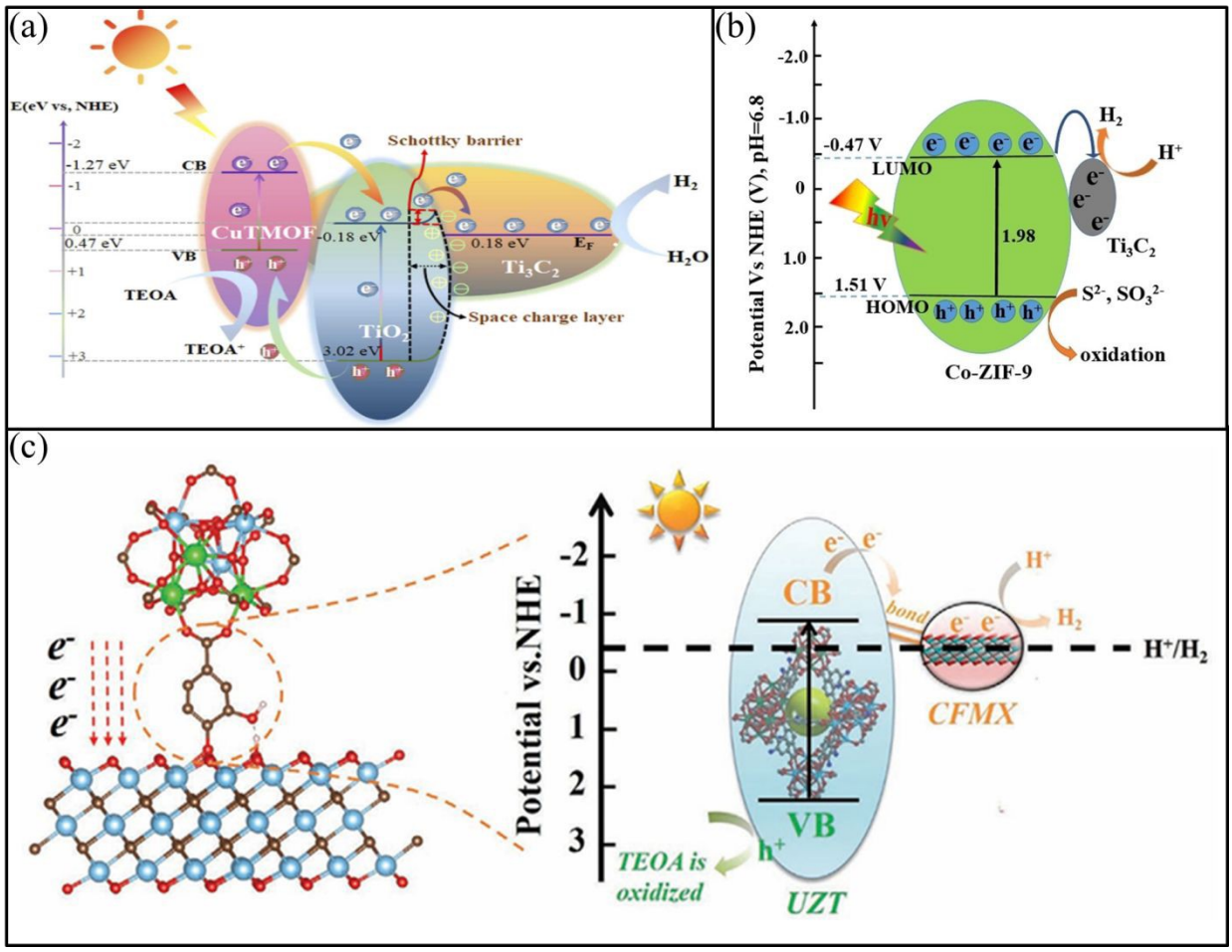

View Article Online
DOI: 10.1039/D5CP02795K

Figure 16. (a) TT/CuTMOF nanocomposite photocatalytic mechanism. Reproduced with permission from.[107] Copyright 2023, Elsevier, (b) Possible photocatalytic mechanism for H_2-evolution over the Co ZIF-9/Ti_3C_2 composite. Reproduced with permission from.[105] Copyright 2022, (c) Schematic of the photocatalytic water splitting mechanism for UZT/CFMX. Reproduced with permission from.[101] Copyright 2022 open access CC BY 4.0

3.3. Energy storage as a supercapacitor by MOF/MXene composites;

Supercapacitors, also known as ultracapacitors or electrochemical capacitors, are energy storage devices that bridge the gap between traditional capacitors and batteries. They store energy through electrostatic double-layer capacitance, enabling high power density and rapid charging/discharging capabilities.[112] With their ability to deliver high power pulses, supercapacitors are suitable for applications requiring rapid energy storage and release. They also boost a long cycle life, withstanding millions of charge/discharge cycles, and can charge discharge quickly.[113] These properties make supercapacitors ideal for various applications, including energy storage. By storing energy generated from the renewable sources and releasing it when needed, supercapacitors can help improve energy efficiency and reduce our reliance on fossil fuels.[26] For example, Wei et al. (2024) prepared MXene@NiCo-MOF nanocomposite and act as anode **(Figure 17a).** The prepared nanomaterial surface area was 50.63 m^2 g^{-1}. The synthesized nanocomposite had the energy density and power density 40.23 Wh kg^{-1}, and 1495.07 W kg^{-1} respectively. The capacitance of the prepared nanocomposite was 2720 (F g^{-1}) at current density of 1 A g^{-1}, respectively **(Figure 17b).** The capacitance retention was found to be 93.21 % after 10,000 cycles **(Figure 17c).** The electrolyte used in MXene@NiCo-MOF was 2 M KOH.[114] **Table 4.** Depicting the MXene/MOF based supercapacitors.

View Article Online
DOI: 10.1039/D5CP02795K

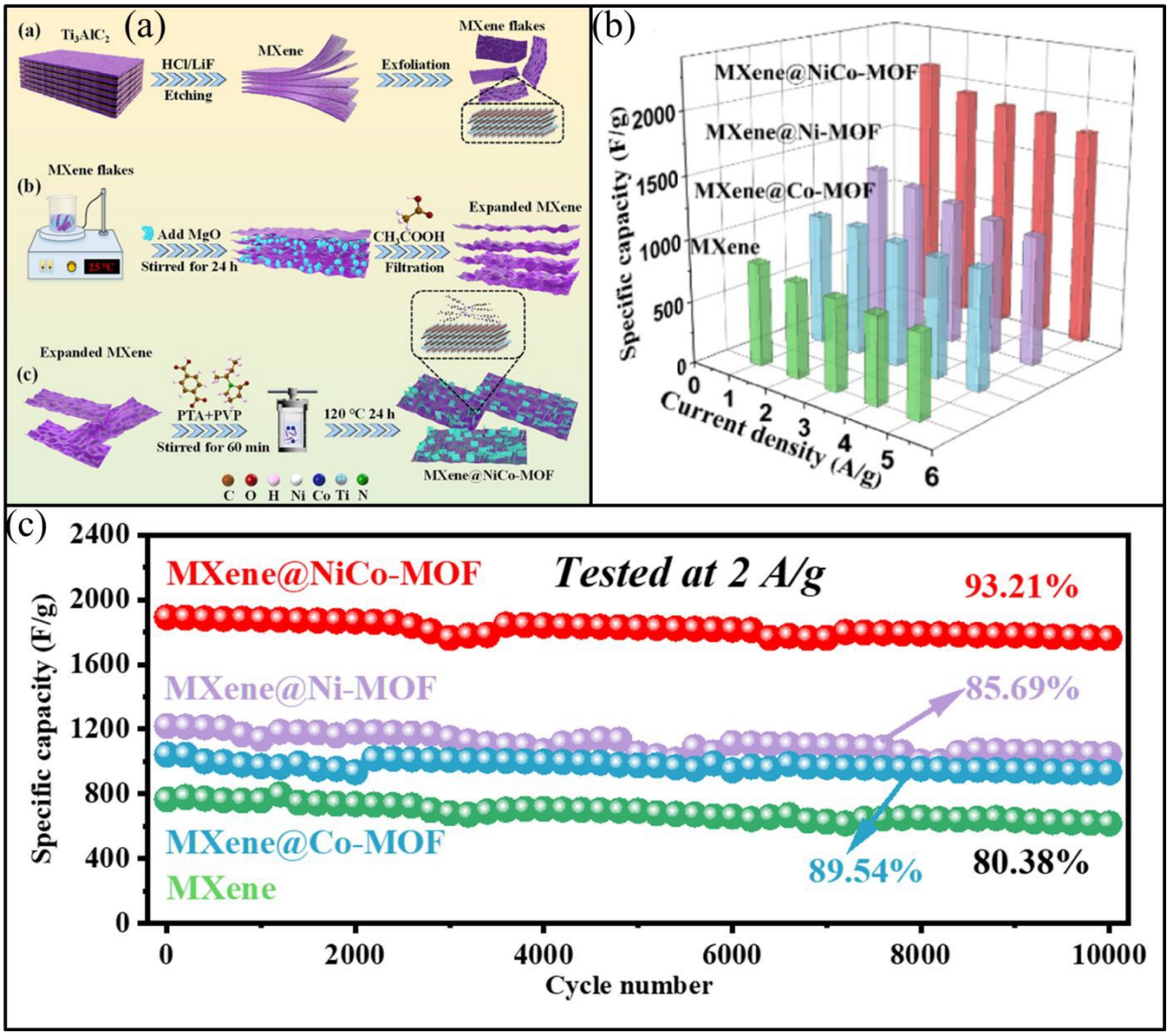

Figure 17. (a) A simplified representation of fabrication method of the MXene@NiCo-MOF, (b) Specific capacitance of four electrodes, and (c) cycling stability for 10000 cycles of as-prepared electrode. Reproduced with permission from.[114] Copyright 2024, Elsevier.

Lu et al. (2022) Synthesized M-$NiCo_2O_4$@NiCo-MOF/CC nanocomposite and as anode for supercapacitor through hydrothermal approach and electrodeposition process. The synthesized nanocomposite had the power density and energy density 750 W kg g^{-1}, and 56.7 Wh kg^{-1} respectively. The capacitance of the prepared nanomaterials was 2091.0 F g^{-1} at current density of

View Article Online
DOI: 10.1039/D5CP02795K

1 A g^{-1}. The capacitance retention was found to be 90.3% after 6000 cycles. The electrolyte used in M-$NiCo_2O_4$@NiCo-MOF/CC was 3 M KOH. Thakur et al.[26] synthesized $Ti_3C_2T_x$/Ni-MOF nanocomposite through solvothermal method for its use as an electrode material for supercapacitor **(Figure 18a).** The surface area of the synthesized nanomaterial was 166 m^2 g^{-1}. The power density and energy density of the prepared nanomaterial were 331.8 W kg^{-1}, and 19.4 Wh kg^{-1}, respectively. The capacitance of the synthesized nanocomposite was 139.4 F g^{-1} at current density of 1 A g^{-1}, respectively **(Figure 18b).** Capacitance retention was determined to be 95 % after 5000 cycles **(Figure 18c).** Polyvinyl alcohol in 1 M H_2SO_4 was used as an electrolyte.

View Article Online
DOI: 10.1039/D5CP02795K

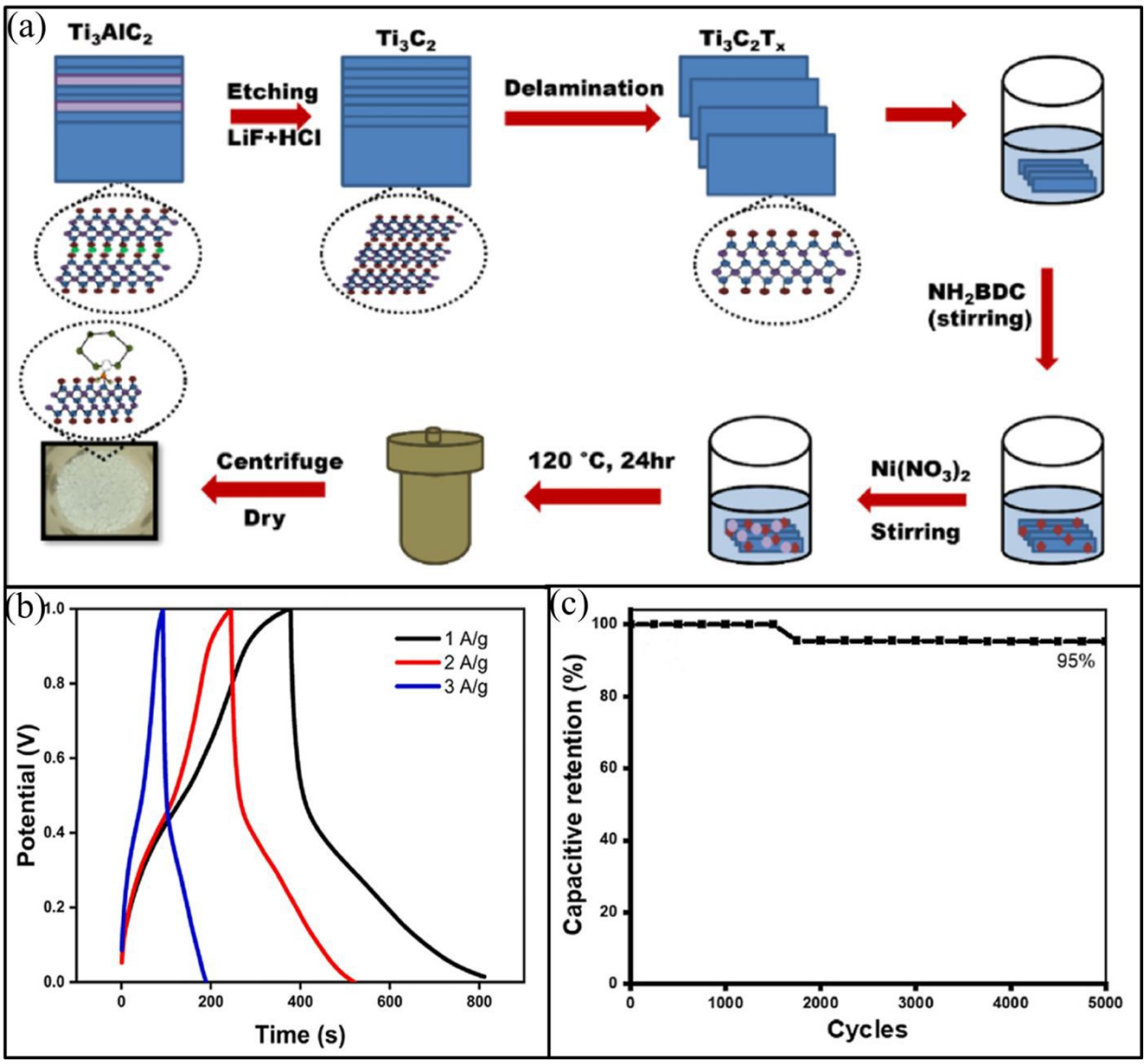

Figure 18. (a) Schematic representation of the synthesis of Ti_3C_2Tx/Ni-MOF composite, (b) GCD curve of Ti_3C_2Tx/Ni-MOF composite at varied current densities, and (c) Cyclic stability performance of the device. Reproduced with permission from.[26] Copyright 2024, Elsevier.

Shivade et al.[27] used a solvothermal approach to synthesized Ni-MOF/MXene composite as a positive electrode for supercapacitor. They employed folic acid as a biological organic linker, in the preparation of Ni- MOF/MXene composite. The power density and energy density of the prepared nanocomposite were 2.841 KW kg^{-1}, and 23.28 Wh kg^{-1}, respectively. The synthesized

View Article Online
DOI: 10.1039/D5CP02795K

Ni-MOF/ MXene composite has a current density of 1 A/g, in a 1 M KOH electrolyte and current density capacitance of 716.19 F g^{-1}, respectively. The capacitance retention was found to be 97.84 % after 2000 cycles. Shalini et al.[56] prepared 100 MX-MN nanocomposites as a positive electrode using hydrothermal method **(Figure 19a)**. (Shalini et al., 2024) used numerous ratios of MX such as 50 mg, 75 mg, 100 mg, and 150 mg were prepared and termed 50 MX-MN, 75 MX-MN, 100 MX-MN, and 150 MX-MN, respectively **(Figure 19b).** BET surface area of 100 MX-MN was 251. 77 $m^2 g^{-1}$ **(Figure 19c).** When compared to other materials, the materials with highest surface area showed best electrochemical properties. Electrochemical procedures such as GCD and CV were carried out. Specific capacity of 100 MX-MN composite was 1028 C g^{-1} at current density 1 A g^{-1}, respectively. The specific capacity of all composite at 1 A g^{-1} were given in **(Figure 19d).** The energy density of 100 MX-MN was 87. 35 W h kg^{-1} and power density 1.98 kW kg^{-1}, respectively. After 10,000 cycles 88% was the capacity retention.

View Article Online
DOI: 10.1039/D5CP02795K

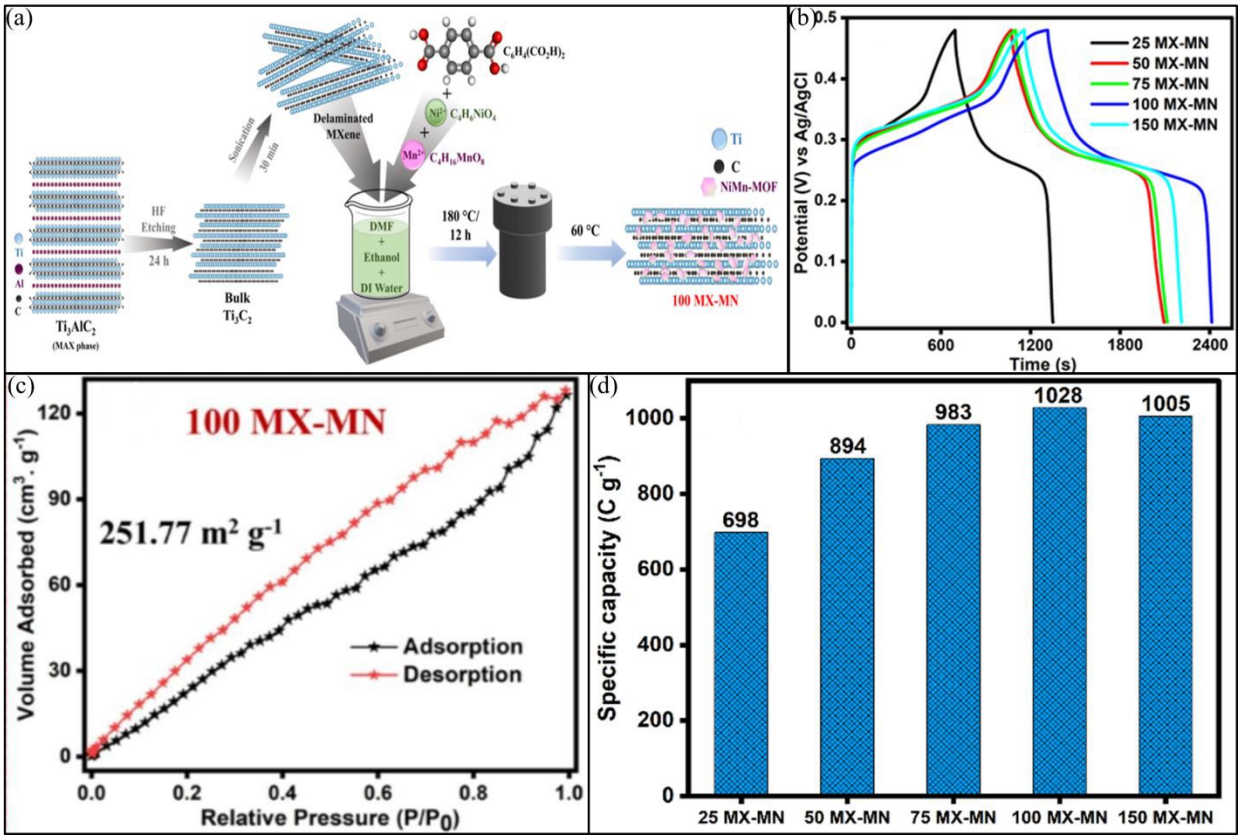

Figure 19. (a) The schematic representation of etching aluminum from MAX phase and synthesis of composites. (b) the GCD cure at 1 A g^{-1}, (c) The nitrogen adsorption- desorption and pore distribution curves of the 100 MX- MN composite, and (d) specific capacity of all the composite at 1 A g^{-1} Reproduced with permission from.[56] Copyright 2024, Elsevier.

Table 4. Summary of MOF/MXene composites for supercapacitor

MOF/MXene composite	Electrolyte	Surface area (m^2/g)	Capacitance	Current density/Scan rate (A g^{-1})	Energy density (Whk g^{-1})	Power density (Wk g^{-1})	Capacitance retention (Cycles)	Reference
CA@MIL-101-(Cr)/Ti3C2T	KOH	208	2720 (F g^{-1})	1.5	38	1280	84% / 10,000	115
MXene@NiCo-MOF	2 M KOH	50.63	2078.1 F·g^{-1}	2	40.23	1495.07	93.21%/10,000	114
MIL-100(Fe)/Ti_3C_2	KOH	529.49	962.17 F g^{-1}	0.5	85.53	200	93% / 10,000	116
MOF/MXene/NF-300//AC/NF	1 M KOH		2453 F/g	1	46.3	746.8	118.1%/15,000	117
NiCo-MOF/Ti3C2Tx	2 M KOH	22.56	815.2 A g^{-1}	1	39.5	562.5	82.3%/ 10,000	118
MOF-5/V_2CT_x//AC	3 M KOH	83	235 C/g	2–3.5	48.75	920	95%/ 16,000	119
M-NC@NCM/NF	NiCo solution		2137.5 F g^{-1}	1	32.6	7000	75.3% / 5000	120
$Ti_3C_2T_x$/Ni-MOFs	6 M KOH	96.6	1124 F g^{-1}	1	46	0.8	74.8% /4000	121
CoTC-300//AC	1.0 M KOH		217.3 C cm^{-3})	10 A m^{-2}	176.3	337.5 W L^{-1}	100% /5000	122
Ni/Co-MOF@TCT-NH_2//AC	3.0 M KOH	129.22	1924 F·g^{-1}	0.5	98.1	600	99.3% /15,600	123
Ni-MOF/MXene	1 M KOH		716.19 F/g	1	23.28	2.841	97.84% /2000	27
100 MX-MN	2 M KOH	251. 77	1028 C g^{-1}	1	87. 35	1.98	88% /10,000	56
$Ti_3C_2T_x$/Ni-MOF	Polyvinyl alcohol in 1 M H_2SO_4	166	139.4 F/g	1	19.4	331.8	95% /5000	26
Ni-MOF/$Ti_3C_2T_x$	KOH/PVA	167.74	497.6 F·g^{-1}	0.5	223.9	1953.3	85% /1000	124
MnO_2@Co_3O_4-PC@MX-CNF	PVA/KOH		475.4 mAh g^{-1}	1	72.5	832.4	90.36% /10,000	125

NiCo-LDH/$Ti_3C_2T_x$-5	2 M KOH	121.38	635.7 C g^{-1}	1	44.6	852.5	85.71% /10,000	[126]
NiCo-MOF/Ti_3C_2Tx	2 M KOH	22.56	815.2 F g^{-1}	1	39.5	562.5	82.3% /10,000	[118]
M-$NiCo_2O_4$@NiCo-MOF/CC	3 M KOH		2091.0 F g^{-1}	1	56.7	750	90.3% /6000	[127]
MXene-FeCu MOF@NF	PVA /KOH		460 mA h cm^{-2}	3 mA cm^{-2}	33.3	503	89% /10,000	[128]

View Article Online
DOI: 10.1039/D5CP02795K

4. Conclusion and Future Perspectives

MOF/MXene composites represent a highly promising class of multifunctional materials that synergistically integrate the high porosity, tunable framework, and catalytic versatility of MOFs with the superior electrical conductivity, mechanical strength, and surface functionality of MXenes. This overview provides a comprehensive summary of the synthesis strategies, structural architectures, and practical applications of these hybrids across diverse fields, including energy storage, catalysis, sensing, and environmental remediation. Despite the remarkable progress achieved, several challenges remain that directly influence their large-scale applicability and functional efficiency. The intrinsic instability and limited conductivity of conventional MOFs, combined with the oxidation sensitivity and surface degradation of MXenes, often lead to inconsistent interfacial bonding and compromised electronic pathways. Furthermore, the structural compatibility between MOF frameworks and MXene layers significantly affects ion transport, active site accessibility, and overall charge-transfer efficiency, highlighting the importance of precise interface engineering. Similarly, the selection of metal nodes, organic linkers, and surface terminations plays a decisive role in tuning redox activity and catalytic selectivity. Understanding and optimizing these interfacial and compositional parameters are therefore central to improving performance consistency and device reliability. With rational structural design, advanced synthesis control, and deeper insight into interfacial phenomena, MOF/MXene composites can evolve from promising laboratory materials to practical systems capable of addressing critical challenges in clean energy, environmental sustainability, and advanced sensing technologies.

Future research should prioritize the following essential directions;

Advance materials design; Look beyond traditional ZIF and MIL MOFs to discover new 2D/2D designs and heterostructures that improve charge transfer and increase electrochemical activity.

View Article Online
DOI: 10.1039/D5CP02795K

Interface Engineering; Create strategies for controlled chemical and physical bonding between MOF and MXene, using surface functional groups to create well-ordered heterojunctions.

Green synthesis approaches; Shift to environmentally friendly and scalable fabrication technique to enable industrial-scale manufacturing, abandoning harmful etchants and high- energy procedures.

In- situ characterization and simulation; Use modern in- situ instruments and computer simulations to better understand composite structural evolution, electronic interactions, and real time behavior under operational settings.

Application-Specific Optimization: Modulate factors such as morphology, dimensionality, and surface chemistry to optimize composite structures for improved performance in specific domains such as supercapacitors, photocatalysts and sensors.

Biological and photonic integration: Take advantages of MOF biocompatibility and MXene optical characteristics to create biomedical carriers, SERS platforms and plasmonic devices.

View Article Online
DOI: 10.1039/D5CP02795K

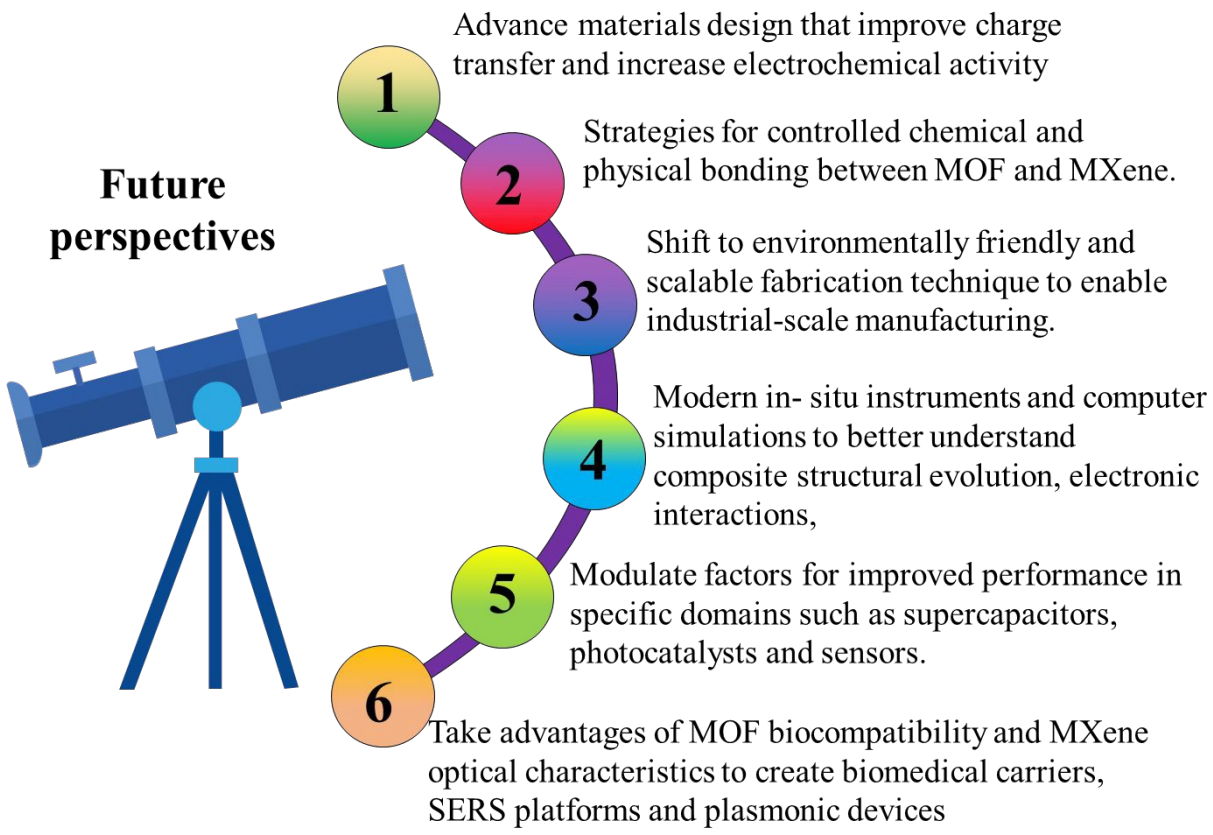

Figure 20. Proposed future research direction for MXene/MOFs composite.

Declarations

Ethics approval and consent to participate: NA

Consent for publication: NA

Data availability: NA

Competing interests: The authors declare no conflict of interest.

View Article Online
DOI: 10.1039/D5CP02795K

Funding: This research received funding from South African Coal, Oil, and Gas Corporation-National Research Foundation (SASOL-NRF) University Collaborative Research Grants (Grant No. 138626)

Authors' contributions:

Muhammad Kashif: Conceptualization, Data curation, Investigation, Methodology, Visualization, Writing – original draft. Syed Izaz Ali Shah: Conceptualization, Validation, Writing – original draft. Salman Khan: Conceptualization, Visualization, Writing – original draft. Sheraz Ahmad: Resources, Writing – review & editing. Muhammad Anwar and Sami Ur Rahman: Resources, Writing – review & editing. Shohreh Azizi: Writing – review & editing. Malik Maaza: Writing – review & editing.

Acknowledgments: The authors thank the SASOL National Research Foundation of South Africa (SASOL NRF) grant RC code 868400 and grant no:138626.

References

1. S. khan, U. Kalsoom, M. Kashif, S. A. Hussain, M. Gul, S. Azizi and M. Maaza, *Water, Air, & Soil Pollution*, 2025, **236**, 900.
2. C. Medjili, N. Lakhdari, D. Lakhdari, A. Berchi, N. Osmani, I. Laourari, Y. Vasseghian and M. Berkani, *Chemosphere*, 2023, **313**, 137427.
3. C. Chinnasamy, N. Perumal, A. Choubey and S. Rajendran, *Environmental Research*, 2023, 116459.
4. H. Bahramian, A. Fattah-alhosseini, M. Karbasi, E. Nikoomanzari and S. Giannakis, *Chemical Engineering Journal*, 2023, **476**, 146588.
5. R. Hosseini, A. Fattah-alhosseini and M. Karbasi, *Surfaces and Interfaces*, 2023, **42**, 103311.
6. A. K. Pandey, D. V. Sarada and A. Kumar, *Proceedings of the National Academy of Sciences, India Section B: Biological Sciences*, 2016, **86**, 805-815.
7. A. Baban, A. Yediler, D. Lienert, N. Kemerdere and A. Kettrup, *Dyes and pigments*, 2003, **58**, 93-98.
8. P. M. Ondarza, S. P. Haddad, E. Avigliano, K. S. Miglioranza and B. W. Brooks, *Science of the total Environment*, 2019, **649**, 1029-1037.
9. H. B. Quesada, A. T. A. Baptista, L. F. Cusioli, D. Seibert, C. de Oliveira Bezerra and R. Bergamasco, *Chemosphere*, 2019, **222**, 766-780.
10. M. Zilker, F. Sörgel and U. Holzgrabe, *Journal of pharmaceutical and biomedical analysis*, 2019, **166**, 222-235.

View Article Online
DOI: 10.1039/D5CP02795K

11. S. Mahapatra, M. H. Ali and K. Samal, *Energy Nexus*, 2022, **6**, 100062.
12. L. A. Schaider, R. A. Rudel, J. M. Ackerman, S. C. Dunagan and J. G. Brody, *Science of the Total Environment*, 2014, **468**, 384-393.
13. S. Webb, T. Ternes, M. Gibert and K. Olejniczak, *Toxicology letters*, 2003, **142**, 157-167.
14. A. Aschengrau, J. M. Weinberg, P. A. Janulewicz, M. E. Romano, L. G. Gallagher, M. R. Winter, B. R. Martin, V. M. Vieira, T. F. Webster and R. F. White, *Environmental health*, 2011, **10**, 1-13.
15. N. Z. Arman, S. Salmiati, A. Aris, M. R. Salim, T. H. Nazifa, M. S. Muhamad and M. Marpongahtun, *Water*, 2021, **13**, 3258.
16. C. Zwiener, *Analytical and bioanalytical chemistry*, 2007, **387**, 1159-1162.
17. F. Dawood, M. Anda and G. Shafiullah, *International Journal of Hydrogen Energy*, 2020, **45**, 3847-3869.
18. R. Rincón, A. Marinas, J. Muñoz, C. Melero and M. Calzada, *Chemical Engineering Journal*, 2016, **284**, 1117-1126.
19. J. D. Holladay, J. Hu, D. L. King and Y. Wang, *Catalysis today*, 2009, **139**, 244-260.
20. M. Tahir, *Energy & Fuels*, 2024.
21. S. C. Hui, 2007.
22. C.-J. Winter, *International Journal of Hydrogen Energy*, 2005, **30**, 681-685.
23. F. Zhang, P. Zhao, M. Niu and J. Maddy, *International journal of hydrogen energy*, 2016, **41**, 14535-14552.
24. N. Serpone, D. Lawless and R. Terzian, *Solar Energy*, 1992, **49**, 221-234.
25. T. Ramachandran, F. Hamed, R. K. Raji, S. M. Majhi, D. Barik, Y. A. Kumar, R. M. Jauhar, M. Pachamuthu, L. Vijayalakshmi and S. Ansar, *Journal of Physics and Chemistry of Solids*, 2023, **180**, 111467.
26. K. K. Thakur, A. L. Sharma and S. Singh, *Materials Chemistry and Physics*, 2024, **322**, 129463.
27. D. S. Shivade, A. N. Kurade, R. K. Bhosale, S. S. Kundale, A. R. Shelake, A. D. Patil, P. P. Waifalkar, R. K. Kamat, A. M. Teli and T. D. Dongale, *Journal of Energy Storage*, 2024, **100**, 113754.
28. J. Xie, C. Yang, M. Duan, J. Tang, Y. Wang, H. Wang and J. Courtois, *Ceramics International*, 2018, **44**, 5459-5465.
29. M. Liu, L. Zhou, X. Luo, C. Wan and L. Xu, *Catalysts*, 2020, **10**, 788.
30. A. N. Hong, H. Yang, X. Bu and P. Feng, *EnergyChem*, 2022, **4**, 100080.
31. W. Peng, L. Han, Y. Gao, Z. Gong, T. Lu, X. Xu, M. Xu, Y. Yamauchi and L. Pan, *Journal of Colloid and Interface Science*, 2022, **608**, 396-404.
32. X. Liu, Y. Shan, S. Zhang, Q. Kong and H. Pang, *Green Energy & Environment*, 2023, **8**, 698-721.
33. S. Lin, Z. Song, G. Che, A. Ren, P. Li, C. Liu and J. Zhang, *Microporous and mesoporous materials*, 2014, **193**, 27-34.
34. T. Qin, Z. Wang, Y. Wang, F. Besenbacher, M. Otyepka and M. Dong, *Nano-Micro Letters*, 2021, **13**, 183.
35. S. K. Sharma, A. Kumar, G. Sharma, D.-V. N. Vo, A. García-Peñas, O. Moradi and M. Sillanpää, *Chemosphere*, 2022, **291**, 132923.
36. Y. Lee, S. J. Kim, Y.-J. Kim, Y. Lim, Y. Chae, B.-J. Lee, Y.-T. Kim, H. Han, Y. Gogotsi and C. W. Ahn, *Journal of Materials Chemistry A*, 2020, **8**, 573-581.
37. Z. Hao, S. Zhang, S. Yang, X. Li, Y. Gao, J. Peng, L. Li, L. Bao and X. Li, *ACS Applied Energy Materials*, 2022, **5**, 2898-2908.
38. X. Yang, Y. Yao, Q. Wang, K. Zhu, K. Ye, G. Wang, D. Cao and J. Yan, *Advanced Functional Materials*, 2022, **32**, 2109479.
39. X. Zhang, X. Liu, Y. Feng, S. Qiu, Y. Shao, Q. Liao, H. Li and Y. Liu, *Applied Materials Today*, 2022, **27**, 101483.
40. W. Qian, Y. Si, P. Chen, C. Tian, Z. Wang, P. Li, S. Li and D. He, *Small*, 2024, **20**, 2403149.

View Article Online
DOI: 10.1039/D5CP02795K

41. U. Kalsoom, S. Khan, M. Kashif, H. S. Yaseen, S. A. Hussain, S. Azizi and M. Maaza, *Ionics*, 2025, DOI: 10.1007/s11581-025-06628-z.
42. S. Venkateswarlu, S. Vallem, M. Umer, N. Jyothi, A. G. Babu, S. Govindaraju, Y. Son, M. J. Kim and M. Yoon, *Journal of Energy Chemistry*, 2023, **86**, 409-436.
43. X. Zhuang, S. Zhang, Y. Tang, F. Yu, Z. Li and H. Pang, *Coordination Chemistry Reviews*, 2023, **490**, 215208.
44. G. Yang and S.-J. Park, *Materials*, 2019, **12**, 1177.
45. T. Ramachandran, A. H. I. Mourad, R. K. Raji, R. Krishnapriya, N. Cherupurakal, A. Subhan and Y. Al-Douri, *International Journal of Energy Research*, 2022, **46**, 16823-16838.
46. M. A. Nazir, M. S. Bashir, M. Jamshaid, A. Anum, T. Najam, K. Shahzad, M. Imran, S. S. A. Shah and A. ur Rehman, *Surfaces and Interfaces*, 2021, **25**, 101261.
47. Z. Hu, Y. Wang and D. Zhao, *Accounts of Materials Research*, 2022, **3**, 1106-1114.
48. B. Liu, K. Vellingiri, S.-H. Jo, P. Kumar, Y. S. Ok and K.-H. Kim, *Nano Research*, 2018, **11**, 4441-4467.
49. A. Nandagudi, S. Nagarajarao, M. Santosh, B. Basavaraja, S. Malode, R. Mascarenhas and N. Shetti, *Materials Today Sustainability*, 2022, **19**, 100214.
50. Y. Pan, J. Wang, X. Guo, X. Liu, X. Tang and H. Zhang, *Journal of colloid and interface science*, 2018, **513**, 418-426.
51. Y. Wu, X. Li, Q. Yang, D. Wang, F. Yao, J. Cao, Z. Chen, X. Huang, Y. Yang and X. Li, *Chemical Engineering Journal*, 2020, **390**, 124519.
52. P. Tian, X. He, L. Zhao, W. Li, W. Fang, H. Chen, F. Zhang, Z. Huang and H. Wang, *International Journal of Hydrogen Energy*, 2019, **44**, 788-800.
53. X. Yu, Y. Hu, X. Luan, S. J. Shah, L. Liu, C. Li, Y. Ren, L. Zhou, J. Li and J. Deng, *Chemical Engineering Journal*, 2023, **476**, 146878.
54. P. Tian, X. He, L. Zhao, W. Li, W. Fang, H. Chen, F. Zhang, Z. Huang and H. Wang, *Solar Energy*, 2019, **188**, 750-759.
55. F. Yang, J. Li, J. Dong, S. Chen, W. Hu, Y. Zhang, H. Wang, Z. Li and Z. Wang, *Separation and Purification Technology*, 2024, **337**, 126488.
56. S. S. Shalini, Y.-P. Fu and A. C. Bose, *Chemical Engineering Journal*, 2024, **500**, 156751.
57. N. Liu, Y. Zheng, C. Jing, B. Gao, W. Huang, Z. Li, J. Lei, X. Zhang, L. Cui and L. Tang, *Journal of Molecular Liquids*, 2020, **311**, 113201.
58. Z.-F. Lin, T.-H. Wang, P. Venkatesan and R.-A. Doong, *Chemical Engineering Journal*, 2025, **505**, 159411.
59. S. Eslaminejad, R. Rahimi and M. Fayazi, *Journal of Industrial and Engineering Chemistry*, 2025, **141**, 94-103.
60. J. Gu, H. Fan, C. Li, J. Caro and H. Meng, *Angewandte Chemie*, 2019, **131**, 5351-5355.
61. W. Xiang, Y. Zhang, H. Lin and C.-j. Liu, *Molecules*, 2017, **22**, 2103.
62. L. Cheng, Y. Tang, M. Xie, Y. Sun and H. Liu, *Journal of Alloys and Compounds*, 2021, **864**, 158913.
63. S. Liu, X. Jiang, G. I. Waterhouse, Z.-M. Zhang and L.-m. Yu, *Separation and Purification Technology*, 2022, **294**, 121094.
64. K. Zhang, Y. Zhu, K. Yue, K. Zhan, P. Wang, Y. Kong, Y. Yan and X. Wang, *Nano Research*, 2023, **16**, 3672-3679.
65. J. Zhu, W. Nie, Q. Wang, J. Li, H. Li, W. Wen, T. Bao, H. Xiong, X. Zhang and S. Wang, *Carbon*, 2018, **129**, 29-37.
66. Z.-Q. Li, L.-G. Qiu, T. Xu, Y. Wu, W. Wang, Z.-Y. Wu and X. Jiang, *Materials Letters*, 2009, **63**, 78-80.
67. H. He, X. Wang, Q. Yu, W. Wu, X. Feng, D. Kong, X. Ren and J. Gao, *Catalysts*, 2023, **13**, 876.
68. H. S. Far, M. Najafi, E. Moradi, M. Atighi, M. Rabbani and M. Hasanzadeh, *Journal of Molecular Structure*, 2024, **1312**, 138627.

View Article Online
DOI: 10.1039/D5CP02795K

69. H. S. Far, M. Najafi, M. Hasanzadeh and R. Rahimi, *Inorganic Chemistry Communications*, 2023, **152**, 110680.
70. H. T. Pham, J. Y. Choi, X. Fang, A. Claman, S. Huang, S. Coates, L. Wayment, W. Zhang and J. Park, *Chem*, 2024, **10**, 199-210.
71. H. T. Pham, J. Y. Choi, M. Stodolka and J. Park, *Accounts of Chemical Research*, 2024, **57**, 580-589.
72. C. Huang, W. Sun, Y. Jin, Q. Guo, D. Mücke, X. Chu, Z. Liao, N. Chandrasekhar, X. Huang and Y. Lu, *Angewandte Chemie International Edition*, 2024, **63**, e202313591.
73. X. Xiao, X. Peng, H. Jin, T. Li, C. Zhang, B. Gao, B. Hu, K. Huo and J. Zhou, *Advanced Materials*, 2013, **25**, 5091-5097.
74. D. Huang, L. Chen, L. Yue, F. Yang, H. Guo and W. Yang, *Journal of Alloys and Compounds*, 2021, **867**, 158764.
75. G. Nagaraju, S. C. Sekhar, B. Ramulu and J. S. Yu, *Energy Storage Materials*, 2021, **35**, 750-760.
76. J. Kim, C. Young, J. Lee, Y.-U. Heo, M.-S. Park, M. S. A. Hossain, Y. Yamauchi and J. H. Kim, *Journal of Materials Chemistry A*, 2017, **5**, 15065-15072.
77. L. Sun, Y. Chen, K. Zhuo, D. Sun, J. Liu and J. Wang, *Electrochimica Acta*, 2023, **466**, 143005.
78. I. Dědek, V. Kupka, P. Jakubec, V. Šedajová, K. Jayaramulu and M. Otyepka, *Applied Materials Today*, 2022, **26**, 101387.
79. P. S. NK, S. M. Jeong and C. S. Rout, *Energy Advances*, 2024, **3**, 341-365.
80. M. Ibrahim, M. G. Fayed, S. G. Mohamed, Z. Wen, X. Sun and H. N. Abdelhamid, *ACS Applied Energy Materials*, 2022, **5**, 12828-12836.
81. H. T. Pham, J. Y. Choi, S. Huang, X. Wang, A. Claman, M. Stodolka, S. Yazdi, S. Sharma, W. Zhang and J. Park, *Journal of the American Chemical Society*, 2022, **144**, 10615-10621.
82. S. Zhou, T. Liu, M. Strømme and C. Xu, *Angewandte Chemie International Edition*, 2024, **63**, e202318387.
83. A. Fattah-alhosseini, Z. Sangarimotlagh, M. Karbasi and M. Kaseem, *Nano-Structures & Nano-Objects*, 2024, **38**, 101192.
84. R. R. Zairov, A. Syed, M. M. Tawfiq, A. F. Al-Hussainy, A. S. Mansoor, U. K. Radi, A. H. Idan, H. Bahair, H. A. Al-Shwaiman and M. Subramaniam, *Spectrochimica Acta Part A: Molecular and Biomolecular Spectroscopy*, 2025, **327**, 125406.
85. D. Wu, Z. Tong, J. Wang, G. Chen, A. Zhu, H. Tong and M. Dang, *Separation and Purification Technology*, 2025, **359**, 130873.
86. Q. Tan, Z. Yu, Q. Xiang, N. He, R. Long and J. Wang, *Process Safety and Environmental Protection*, 2023, **179**, 405-420.
87. Y. Cao, L. Yue, Z. Li, Y. Han, J. Lian, H. Qin and S. He, *Applied Surface Science*, 2023, **609**, 155191.
88. Z. Li, S. Ning, F. Hu, H. Zhu, L. Zeng, L. Chen, X. Wang, T. Fujita and Y. Wei, *Journal of colloid and interface science*, 2023, **629**, 97-110.
89. B. Tan, Y. Fang, Q. Chen, X. Ao and Y. Cao, *Journal of Colloid and Interface Science*, 2021, **601**, 581-593.
90. Z. Fan, X. Zhang, Y. Li, X. Guo and Z. Jin, *Journal of Industrial and Engineering Chemistry*, 2022, **110**, 491-502.
91. K. Yang, T. Liu, D. Xiang, Y. Li and Z. Jin, *Separation and Purification Technology*, 2022, **298**, 121564.
92. S. Rafiq, S. Awan, R.-K. Zheng, Z. Wen, M. Rani, D. Akinwande and S. Rizwan, *Journal of Magnetism and Magnetic Materials*, 2020, **497**, 165954.
93. V. Q. Hieu, T. K. Phung, T.-Q. Nguyen, A. Khan, V. D. Doan, V. A. Tran and V. T. Le, *Chemosphere*, 2021, **276**, 130154.
94. S. I. A. Shah, W. Ahmad, M. Anwar, R. Shah, J. A. Khan, N. S. Shah, A. Al-Anazi and C. Han, *Applied Catalysis O: Open*, 2025, 207049.

View Article Online
DOI: 10.1039/D5CP02795K

95. I. Vamvasakis, A. Trapali, J. Miao, B. Liu and G. S. Armatas, *Inorganic Chemistry Frontiers*, 2017, **4**, 433-441.
96. L. Sun, Q. Shao, Y. Zhang, H. Jiang, S. Ge, S. Lou, J. Lin, J. Zhang, S. Wu and M. Dong, *Journal of colloid and interface science*, 2020, **565**, 142-155.
97. T. Ramachandran, R. K. Raji and M. d. Rezeq, *Journal of Materials Chemistry A*, 2025, **13**, 12855-12890.
98. B. Tahir, A. Alraeesi and M. Tahir, *Frontiers in Chemistry*, 2024, **12**, 1448700.
99. M. Cabrero-Antonino, A. Uscategui-Linares, R. Ramírez-Grau, P. García-Aznar, G. Sastre, J. Zhang, S. Goberna-Ferrón, J. Albero, J. Yu and H. García, *Angewandte Chemie International Edition*, 2025, e202503860.
100. A. Rajan, M. Daniel, J. Rafi, A. S. C. Lazuli and B. Neppolian, *ChemSusChem*, 2025, **18**, e202400207.
101. L. Shi, C. Wu, Y. Wang, Y. Dou, D. Yuan, H. Li, H. Huang, Y. Zhang, I. D. Gates and X. Sun, *Advanced Functional Materials*, 2022, **32**, 2202571.
102. V.-A. Thai, T.-B. Nguyen, C.-W. Chen, X.-T. Bui, R.-a. Doong and C.-D. Dong, *Environmental Science: Nano*, 2024, **11**, 3871-3886.
103. S. Zhang and C. Bie, *Rare Metals*, 2025, 1-4.
104. Y. Li, Y. Liu, Z. Wang, P. Wang, Z. Zheng, H. Cheng, Y. Dai and B. Huang, *Chemical Engineering Journal*, 2021, **411**, 128446.
105. Y. Sun, M. Xie, H. Feng and H. Liu, *ChemPlusChem*, 2022, **87**, e202100553.
106. J.-H. Zhao, L.-W. Liu, K. Li, T. Li and F.-T. Liu, *CrystEngComm*, 2019, **21**, 2416-2421.
107. Y. Chen, H. Zhu, S.-Z. Kang, T. Zhang, L. Qin and X. Li, *Journal of Alloys and Compounds*, 2023, **961**, 170929.
108. L. Biswal, S. P. Tripathy, S. Dash, S. Das, S. Subudhi and K. Parida, *Materials Advances*, 2024, **5**, 4452-4466.
109. H. Zhu, Y. Chen, T. Zhang, L. Qin, S.-Z. Kang and X. Li, *Journal of Solid State Chemistry*, 2023, **327**, 124298.
110. M. J. Molaei, *Fuel*, 2024, **365**, 131159.
111. J. Ke, F. He, H. Wu, S. Lyu, J. Liu, B. Yang, Z. Li, Q. Zhang, J. Chen and L. Lei, *Nano-Micro Letters*, 2021, **13**, 1-29.
112. T. Ramachandran, R. K. Raji, S. Palanisamy, N. Renuka and K. Karuppasamy, *Journal of Industrial and Engineering Chemistry*, 2025, **145**, 144-168.
113. A. M. Bogale, T. Ramachandran, M. E. Suk, B. B. Badassa, M. M. Solomon, J. He, A. Yusuf, R. K. Raji, B. A. Zenebe and N. K. Amare, *Journal of Physics and Chemistry of Solids*, 2025, 113079.
114. J. Wei, F. Hu, Y. Pan, C. Lv, L. Bian and Q. Ouyang, *Chemical Engineering Journal*, 2024, **481**, 148793.
115. H. Hassan, K. Khan, S. Mumtaz, A. A. Rafi, A. M. Idris, A. Althobaiti and A. Mohammad, *Journal of Power Sources*, 2024, **623**, 235486.
116. B. Jia, H. Yang, L. Wang, Z. Zhao and X. Wu, *Applied Surface Science*, 2022, **602**, 154386.
117. X. Yang, Y. Tian, S. Li, Y.-P. Wu, Q. Zhang, D.-S. Li and S. Zhang, *Journal of Materials Chemistry A*, 2022, **10**, 12225-12234.
118. Y. Wang, Y. Liu, C. Wang, H. Liu, J. Zhang, J. Lin, J. Fan, T. Ding, J. E. Ryu and Z. Guo, *Engineered Science*, 2020, **9**, 50-59.
119. H. Hassan, E. Umar, M. W. Iqbal, H. Alrobei, A. M. Afzal, A. K. Alqorashi, T. Yaseen and M. A. Sunny, *Electrochimica Acta*, 2024, **489**, 144277.
120. J. Wang, J. Gong, H. Zhang, L. Lv, Y. Liu and Y. Dai, *Journal of Alloys and Compounds*, 2021, **870**, 159466.
121. X. Zhang, S. Yang, W. Lu, D. Lei, Y. Tian, M. Guo, P. Mi, N. Qu and Y. Zhao, *Journal of Colloid and Interface Science*, 2021, **592**, 95-102.

View Article Online
DOI: 10.1039/D5CP02795K

122. X. Yang, C. Xu, S. Li, Y.-P. Wu, X.-Q. Wu, Y.-M. Yin and D.-S. Li, *Journal of Colloid and Interface Science*, 2022, **617**, 633-640.
123. L. Yue, L. Chen, X. Wang, D. Lu, W. Zhou, D. Shen, Q. Yang, S. Xiao and Y. Li, *Chemical Engineering Journal*, 2023, **451**, 138687.
124. S. Li, Y. Wang, Y. Li, J. Xu, T. Li and T. Zhang, *Nanomaterials*, 2023, **13**, 610.
125. T. Kshetri, D. D. Khumujam, T. I. Singh, Y. S. Lee, N. H. Kim and J. H. Lee, *Chemical Engineering Journal*, 2022, **437**, 135338.
126. Y. Wang, C. Shi, Y. Chen, D. Li, G. Wu, C. Wang and L. Guo, *Electrochimica Acta*, 2021, **376**, 138040.
127. J. Lu, J. Wang, J. Gong and C. Hu, *Journal of Materials Science: Materials in Electronics*, 2022, **33**, 18922-18937.
128. M. Adil, A. G. Olabi, M. A. Abdelkareem, H. Alawadhi, A. Bahaa, K. ElSaid and C. Rodriguez, *Journal of Energy Storage*, 2023, **68**, 107817.

View Article Online
DOI: 10.1039/D5CP02795K

Data Availability Statement : Not applicable , This is a review article and does not contain original data.